Green Chemical Technology

SCIEPublish

Review

Bubbling Fluidized Bed Reactors for CaO-Based CO_2 Capture with Geldart Group B Particles: A Critical Review of the Coupling Between Bubble Hydrodynamics, High-Temperature Heat Transfer and Carbonation Performance

Asim Aamir [1,2,*]

[1] State Key Laboratory of Mesoscience and Engineering, Institute of Process Engineering, Chinese Academy of Sciences, Beijing 100190, China

[2] School of Chemical Engineering, University of Chinese Academy of Sciences, Beijing 100049, China

* Corresponding author. E-mail: asimaamir@ipe.ac.cn (A.A.)

Received: 24 August 2026; Revised: 24 September 2026; Accepted: 21 October 2026; Available online: 2 November 2026

ABSTRACT: Bubbling fluidized beds are used in calcium looping for sorbent testing, thermochemical energy storage, and selected carbon-capture and sorption-enhanced processes. Their performance depends on gas distribution between bubbles and emulsion, the evolving properties of $CaO/CaCO_3$ particles, sorbent circulation, and heat removal. This critical narrative review examines these interactions for particles exhibiting Geldart Group B behaviour. Coupled fluidized-reactor modelling is established, including earlier bubbling-bed calcium-looping models; the contribution here is a synthesis of that literature with transparent screening calculations and an evidence-based validation agenda. A four-constraint representation organizes equilibrium; interphase transport; kinetics and sorbent supply; and thermal feasibility at a specified operating state. The constraints interact, and their minimum is not a substitute for a coupled reactor solution. Calculations account for gas-flow contraction, compare alternative bubble-growth correlations, and examine sensitivity to interchange coefficients, bubble-size distributions, and immersed internals. A reduced coupled example illustrates how finite kinetics and thermal feedback can lower capture below separate limiting estimates. Conversion-dependent particle properties are represented by a conditional constant-envelope calculation and contrasted with measurements of fluidization, bulk density, and fragmentation. Bubble growth can limit capture, but the binding constraint depends on operating conditions and available sorbent. Likewise, the relationship between bubbling and bed-to-surface heat transfer is regime dependent. Reproducible calculations and plotting data accompany the review, and a proposed validation programme identifies the simultaneous measurements needed to evaluate these screening concepts in hot reacting beds.

Keywords: Bubbling fluidized bed; Calcium looping; CaO sorbent; Geldart Group B; Bubble dynamics; High-temperature heat transfer; CO_2 capture; Reactor scale-up

© 2026 The authors. This is an open access article under the Creative Commons Attribution 4.0 International License (https://creativecommons.org/licenses/by/4.0/).

1. Introduction

1.1. Motivation

Carbon capture from flue gas, from process gas and increasingly from air must be delivered at a cost and an energy penalty that industry will tolerate. Among the solid-looping routes, the calcium looping (CaL) cycle is the reversible carbonation of CaO and calcination of $CaCO_3$,

$$CaO_{(s)} + CO_{2(g)} \rightleftharpoons CaCO_{3(s)}, \qquad \Delta H_r^\circ \approx -178\ \mathrm{kJ \cdot mol^{-1}}$$

Calcium looping uses an abundant limestone precursor and operates at temperatures at which carbonation heat can be recovered for useful process or power-generation duties. Integration with cement production can provide a route for using the purge solids. These advantages motivate continued reactor development, although the overall energy penalty and cost depend on heat integration, regeneration conditions, sorbent replacement, and the composition of the treated gas. No general economic ranking of calcium looping against other capture technologies is assumed in this review.

The technology has been demonstrated. Post-combustion CaL has been operated continuously at the 1–2 MWth scale in circulating fluidized bed (CFB) configurations at La Pereda and TU Darmstadt, with stable operation and CO_2 capture efficiencies above 90% reported at La Pereda [1,2].

1.2. Why the Bubbling Regime, and Why Now

The demonstrated dual-CFB configuration is an important reference for post-combustion capture. Bubbling beds nevertheless serve several distinct roles, for which the required solids inventory, residence time, heat-transfer surface, and gas throughput differ.

(i) Thermochemical energy storage. In CaL systems integrated with concentrated solar power, the carbonator releases stored heat and the calciner receives heat. Dense beds offer opportunities for immersed heat exchange and particle mixing. Directly irradiated bubbling beds are one investigated solar-reactor configuration; their surface renewal and radiative boundary conditions require application-specific assessment [3].

(ii) Distributed capture and dilute streams. Reactor selection at smaller or dispersed sources depends on gas throughput, pressure drop, and the arrangement of regeneration and solids transport. Decoupled calcium-looping concepts motivate consideration of dense-phase reactors, but evidence from moving-bed pilots should not be interpreted as validation of bubbling beds [4].

(iii) Sorption-enhanced processes. Combining CaO with a catalyst or fuel can shift reaction equilibria through *in-situ* CO_2 removal. A bubbling carbonator can form part of a dual-fluidized-bed system, although solids residence time, segregation, and cross-contamination must be assessed for the specific configuration [5].

(iv) Kinetics and screening. Micro-fluidized-bed thermogravimetry provides an alternative to conventional thermogravimetric analysis and can reduce sample-scale transport limitations. Wang et al. [6] coupled such measurements to a two-phase bubbling-bed model. Reliable kinetic identification still requires checks for gas delivery, wall effects and minimum fluidization; no claim is made that this technique has replaced conventional TGA throughout the field.

1.3. Why Geldart Group B Is Not an Incidental Detail

Many limestone-derived sorbents in the size range used in dense fluidized beds exhibit Geldart Group B behaviour. Classification depends on particle size, envelope density, gas properties, temperature and the fines fraction, rather than chemical identity alone [7]. The following features describe the classical Group B regime and provide a starting point for interpreting hot reacting beds.

Bubbles generally appear close to incipient fluidization, unlike the wider homogeneous-expansion interval associated with many Group A powders. Hot or confined limestone beds can depart from this simple classification.

Coalescence can produce substantial bubble growth without the material-dependent stable-size mechanism associated with Group A. This does not imply unbounded bubble size in a real vessel: column diameter, slugging, breakup, internals and the operating regime impose additional limits.

For the fast-bubble conditions considered in the classical bubble–cloud–emulsion description, bubble gas exchanges with the surrounding phases over a finite residence time. Whether this closure is appropriate must be checked against local hydrodynamics.

The ideal two-phase approximation assigns the gas flow at minimum fluidization to the emulsion and the excess flow to bubbles. Experiments show emulsion expansion and through-flow, so this division is a closure assumption rather than an exact gas balance for every freely bubbling bed [8,9].

Gas that reaches the outlet without adequate contact with active sorbent lowers capture. The importance of this bypass relative to equilibrium, finite reaction rates and sorbent supply must be established for each reactor. The idealized solids-free bubble phase is used below as a screening assumption.

1.4. What This Review Does Differently

Coupled fluidized-reactor modelling has a long history. Theologos and Markatos [10] solved three-dimensional two-phase flow and heat transfer in FCC risers, and their subsequent work incorporated chemical reaction [11,12]. These studies concern different operating regimes and chemistry, but establish that coupling itself is not a new concept. Recent CaL reviews emphasize sorbent development, process integration and technology maturity [13,14]. The contribution here is a CaL-specific critical synthesis of how bubble-scale transport, thermal management and an evolving sorbent population interact in Geldart-B bubbling beds.

Coupled reactor modelling is established in calcium looping. Shimizu et al. [15] already combined a bubbling-bed absorber model with material and heat balances and found that heat-recovery tube arrangement could govern the required bed height. Later carbonator models incorporated hydrodynamics, sorbent conversion, inventory, and circulation in increasingly detailed CFB descriptions, while reactive BFB simulations now include immersed surfaces [16–18]. Consequently, neither hydrodynamics–reaction coupling nor recognition of thermal constraints is claimed as new here. This review contributes a BFB-focused synthesis that connects bubble–emulsion exchange, evolving particle properties, and immersed-surface heat removal using transparent, conditional screening calculations and an explicit validation agenda.

The organising thesis of this review is:

Bubble statistics link gas–solid contacting and surface renewal, but bubble diameter is not the sole control variable. The effect of increasing gas velocity or changing bubble size on heat transfer can reverse with particle properties, tube geometry and temperature. The design question is therefore a regime-dependent interaction between transport, reaction, solids management and heat removal.

The review organizes these interactions using four coupled constraints evaluated at an explicitly stated operating condition: equilibrium, interphase transport, kinetics and sorbent supply, and thermal feasibility. A conditional screening statement is

$$E \leq \min\left(E_{\mathrm{eq}}, E_{\mathrm{h},0}, E_{\mathrm{rxn/supply}}\right)$$

Here the capture bounds are conditional on the stated closures and operating state; the thermal requirement is an energy-balance feasibility condition. The phrase four-ceiling framework is retained as a descriptive classification, without a claim that the constituent limits or their coupling are new. Figure 1 shows the process context, and Section 6 explains the limits of taking the minimum of separately evaluated bounds.

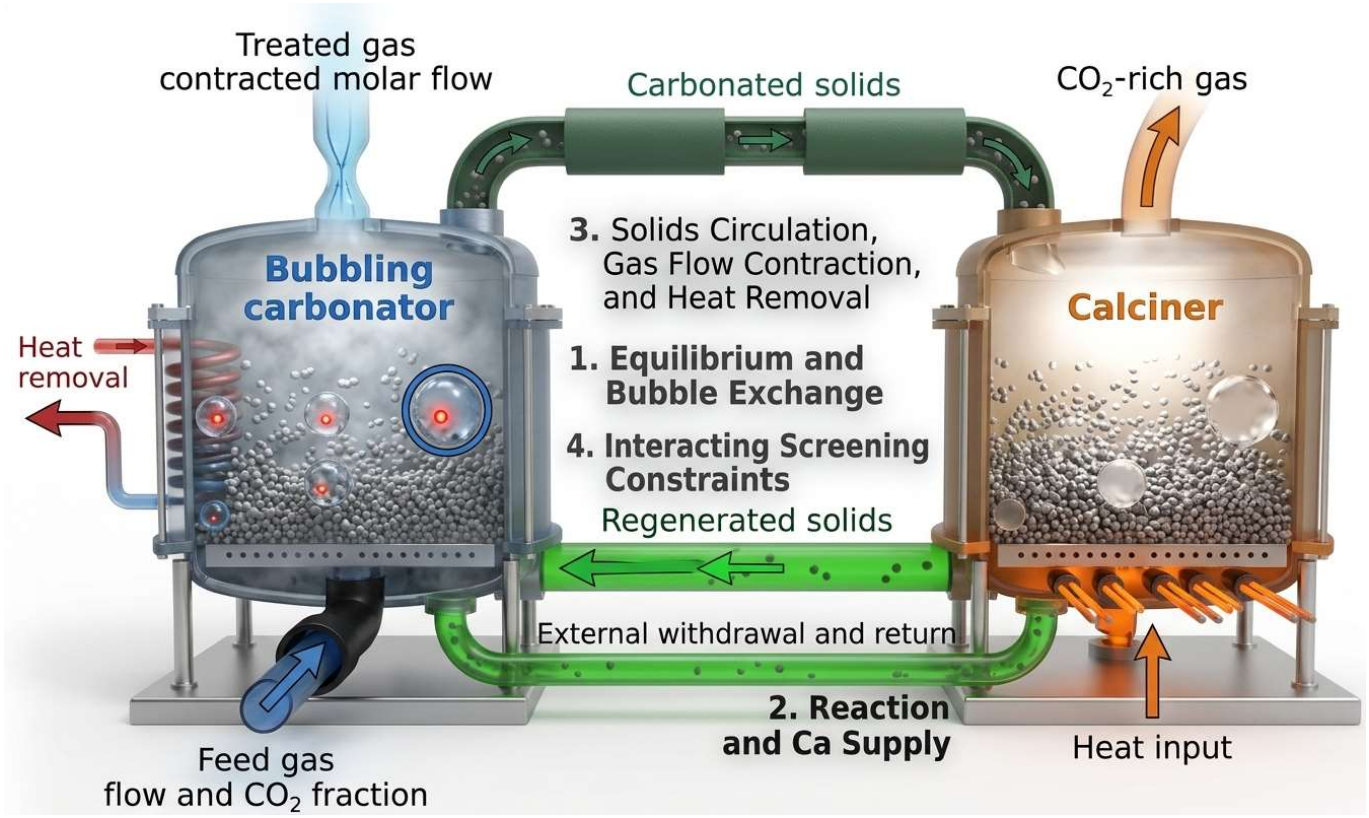


Figure 1. Process context for a bubbling carbonator connected to a calciner and an external solids return. Equilibrium, bubble exchange, reaction and Ca supply, and the energy balance form four interacting screening constraints. Solids circulation, gas-flow contraction and heat removal must be resolved for the same operating state; the diagram does not specify an industrial design.

A second organizing concept is the dynamic Geldart trajectory (Section 2.4), which represents the evolution of particle-envelope density and size with conversion and cycling. Its fixed-envelope calculation is an idealized scenario, while a working reactor contains a distribution of particle sizes, conversions, and cycle histories. Reaction-dependent particle properties have already been incorporated into fluidized-reactor models in other applications, including variable-density biomass gasification [19]. The CaL-specific question is how measured morphology, attrition and conversion distributions should enter and validate the relevant momentum and transport closures; no priority claim is made for variable-density modelling itself.

1.5. Review Scope and Evidence Selection

This article is a critical narrative review supplemented by illustrative calculations, rather than a systematic review or a validated new reactor model. The submitted version reported a CaL-focused search through 24 August 2026. A targeted revision search on 27 September 2026 extended coverage to historical and adjacent applications using combinations of reacting fluidized bed, two-phase fluidized reactor model, fluidized-bed heat and mass transfer, CFD reacting gas-solid flow, fluid catalytic cracking, fluidized-bed drying, reacting DEM, variable particle density and coarse-grained CFD–DEM. Title and author searches, and backward reference tracing were used to identify primary studies; publisher and institutional records were then checked. The supplementary search log records the actual queries and access limitations.

Evidence was selected for its relevance to thermodynamics/kinetics, particle-property evolution, bubble-scale transport, or thermal design. The source record distinguishes (a) measurements in reacting CaO bubbling beds, (b) measurements in inert Group-B bubbling beds, (c) evidence from other reacting fluidized systems, and (d) model-based inference. Non-fluidized sorbent-property measurements are identified separately as supporting evidence. Accessible full texts were used where available; when only a primary publisher abstract or institutional record could be examined, conclusions were restricted to the

information established there. This targeted search cannot establish exhaustive absence or priority, so remaining gaps are framed as needs for CaL-specific evidence and validation.

1.6. Structure

Section 1.5 defines the evidence-selection approach. Section 2 establishes the CaO–CO_2 properties relevant to fluidization. Section 3 reviews Group B hydrodynamics, including temperature and reaction effects. Section 4 examines the condition dependence and uncertainty of high-temperature heat transfer. Section 5 reviews carbonation performance and transport limitations. Section 6 compares conditional constraints and a reduced coupled model. Section 7 proposes validation priorities, and Section 8 concludes.

2. The CaO–CO_2 System from a Reactor-Engineering Standpoint

2.1. Thermodynamics: The First Ceiling

Equilibrium for the CaO/$CaCO_3$ pair has been studied since the work of Baker [20]. The expression used for the baseline calculation is the Silcox et al. [21] representation, with T in kelvin and p_{eq} in atmospheres:

$$p_{eq}/\text{atm} = 4.137 \times 10^7 \exp(-20{,}474/T)$$

$$y_{out} = \frac{y_{in}(1-E)}{1-y_{in}E}, E_{eq} = \max\left[0, \frac{y_{in}-y_{eq}}{y_{in}(1-y_{eq})}\right]$$

Here $E = \frac{F_{CO_2,in} - F_{CO_2,out}}{F_{CO_2,in}}$, $y_{eq} = p_{eq}/P$, and inert molar flow is conserved. If $y_{eq} \geq y_{in}$, there is no positive equilibrium carbonation capture. For $y_{eq} \geq 1$, the carbonation screen is set to zero. Steam condensation, leakage, and other gas reactions are excluded from this balance.

$$p_{eq}/\text{bar} = 4.0009 \times 10^7 \exp\left(\frac{-169{,}500}{RT}\right)$$

The latter is the published FactPS-derived fit in Hornberger et al. [22], reported over 500–1000 °C. It is an independent published representation, not a new database calculation. Conversion uses 1 bar = 100,000 Pa and 1 atm = 101,325 Pa. At 650 °C and 15% inlet CO_2, the bounds are 94.5% and 94.2%; at 700 °C and 4% inlet, they are 25.3% and 21.9%. Extrapolation below the stated fit range, including direct air-capture conditions, is not evaluated here.

Table 1 reports equilibrium concentrations and capture on an inlet CO_2 molar-flow basis. Values are rounded to match the screening purpose. The independent equilibrium comparison and numerical data are provided in the Supplementary Information.

Table 1. Equilibrium composition and capture bounds at 1 atm. Each paired entry is Silcox et al. [21]/the FactPS-derived fit reported by Hornberger et al. [22]; the separation is model sensitivity, not a confidence interval.

T (°C)	Equilibrium CO_2 (vol %)	E_{eq} at 15% Inlet	E_{eq} at 4% Inlet
500	0.0131/0.014	99.9%/99.9%	99.7%/99.7%
550	0.0653/0.0693	99.6%/99.6%	98.4%/98.3%
575	0.136/0.144	99.2%/99.2%	96.7%/96.5%
600	0.271/0.286	98.5%/98.4%	93.5%/93.1%
650	0.965/1.01	94.5%/94.2%	76.6%/75.4%
700	3.02/3.15	82.4%/81.6%	25.3%/21.9%
750	8.44/8.77	47.8%/45.5%	0.0%/0.0%
800	21.4/22.2	0.0%/0.0%	0.0%/0.0%

Equilibrium sets a temperature-dependent limit even when the sorbent remains active and gas–solid transport is rapid. Because CO_2 removal reduces the total gas flow, the capture fraction must be calculated from a molar balance, not from the ratio of outlet and inlet mole fractions alone. The correction is included in Table 1 and Figure 2. High capture in continuous CaL operation additionally requires adequate active inventory and circulation [1,2].

For dilute inlet streams, an increase in equilibrium CO_2 partial pressure consumes a larger fraction of the available driving force. Lower carbonation temperature can therefore improve the equilibrium limit, but the accompanying change in reaction rate must be included. Operation at 550–600 °C is examined below as a dilute-stream example, rather than prescribed as a universal operating window or extrapolated directly to atmospheric CO_2.

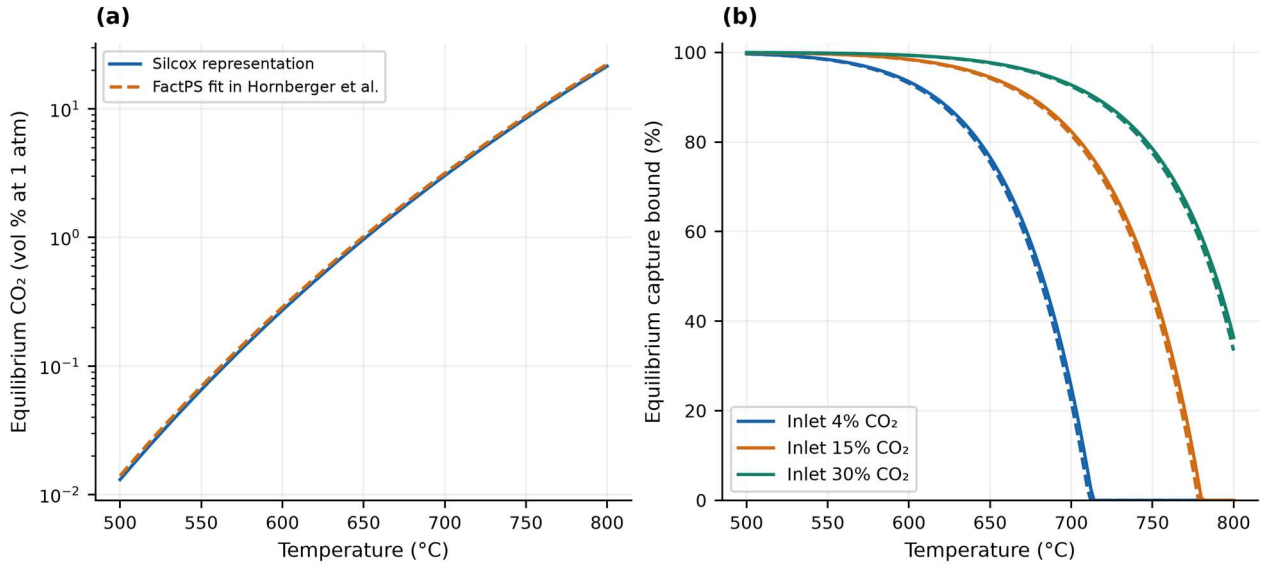


Figure 2. Equilibrium CO_2 concentrations and gas-contraction-corrected capture bounds. (**a**) Equilibrium representations at 1 atm; (**b**) capture on a molar-flow basis for 4%, 15% and 30% inlet CO_2. Solid lines use Silcox et al. [21], and dashed lines use the FactPS-derived fit reported by Hornberger et al. [22], in both panels. Gas contraction is included in (**b**). The source-to-source separation reflects model sensitivity, not a statistical confidence interval. These plots are original calculations using the cited relations; equations, units and plotting data are supplied in the Supplementary Information.

2.2. Kinetics: Two Regimes, One Transition

CaO carbonation commonly exhibits two observable regimes: a rapid surface-reaction stage followed by a slower stage governed by diffusion through, and pore blockage by, the $CaCO_3$ product layer. The transition is often associated with a product layer of roughly 30–50 nm, although its apparent position depends on pore structure, temperature, CO_2 driving force, and the measurement method. The random-pore and product-layer frameworks of Bhatia and Perlmutter [23,24] therefore remain useful reactor closures, but they should not be interpreted as a unique microscopic mechanism across all sorbents and operating conditions.

For reactor modelling, the practically important consequences are:

The accessible conversion depends on the solids residence-time distribution relative to the fast and slower carbonation stages. Active-fraction and active-space-time formulations are useful when the fast stage dominates, but diffusion-controlled uptake can contribute at longer residence times and should not be excluded by definition.

The apparent CO_2 reaction order is regime-dependent rather than universally first order. Near equilibrium and at dilute CO_2 concentrations, the measured order varies with temperature, and experiments can be limited by external CO_2 delivery before intrinsic kinetics are isolated. Fluidized-bed measurements

at 0.38–2.70 vol % CO_2 show that transport screening is essential and that steam accelerates carbonation in the kinetically controlled regime, with diminishing benefit at higher temperatures [25].

The reaction driving force depends on the departure from equilibrium. Consequently, equilibrium and finite kinetics are coupled: a finite reactor generally cannot attain the equilibrium outlet composition exactly. This coupling is retained in the illustrative calculation in Section 6.

Reduced-order kinetic models suitable for embedding in CFD now exist. Analytical reductions of the one-dimensional grain model via the Thiele modulus have been derived and validated against micro-fluidized-bed thermogravimetric data across 600–750 °C, 25–75 vol % CO_2 and particle sizes 0.2–3 mm, capturing the two-stage transition and pore plugging [6]. This is a significant enabler: it makes bubble-resolved reactive simulation tractable.

Calcination should also not be treated simply as the algebraic reverse of a shrinking-core carbonation model. Direct *in-situ* TEM and synchrotron XRD revealed heterogeneous nucleation of stable nanoporous CaO at $CaCO_3$ grain boundaries followed by a planar reaction front, without evidence for the previously proposed metastable expanded CaO intermediate [26]. A complementary first-principles microkinetic formulation couples $CaCO_3$ surface decomposition to nucleation and reproduces measurements across temperature, CO_2 partial pressure, residence time, and particle size [27]. These findings strengthen the case for morphology-aware, thermodynamically consistent kinetics in coupled reactor models.

Micro-fluidized-bed thermogravimetric analysis provides a complementary platform for kinetic measurement. Fluidizing the sample can reduce some transport limitations, but hydrodynamics and wall effects still require assessment. High-temperature tests with Geldart B limestones show that minimum fluidization, bubbling onset, and slugging onset vary with temperature and confinement [28]. Kinetic studies should therefore report geometry, U/U_{mf}, particle loading and transport-limitation checks.

2.3. Deactivation: The Third Ceiling

CaO loses capacity with cycling. The decay is well described by the Grasa–Abanades correlation [29],

$$X_N = \frac{1}{\frac{1}{1-X_r} + kN} + X_r, \qquad k \approx 0.52, X_r \approx 0.075$$

For the natural sorbents and cycling conditions represented by this empirical correlation, the conversion approaches a residual value near 0.075. The coefficients should be fitted or checked for the selected precursor, regeneration atmosphere, and cycle severity; they are not universal material constants. Relevant deactivation mechanisms include the following.

Sintering and crystallite coarsening during calcination reduce porosity and accessible surface area. Direct *in-situ* observations show that high-surface-area nanoporous CaO can form before the higher-temperature coarsening regime becomes dominant, separating CaO formation from subsequent capacity-destroying sintering [26]. Carbonation conversion must therefore be related to the pore network created by the immediately preceding calcination, not to cycle number alone.

Pore plugging in which the 2.2-fold molar volume increase on carbonation seals the pore mouths that give access to the interior.

Sulphation consumes available calcium and can obstruct pores or alter attrition. Its effect depends on sulphur exposure, sorbent history and purge strategy. Coupled kinetic–hydrodynamic modelling has explicitly examined SO_2 effects on calcium-looping carbonators [30]; the corresponding predictions should be transferred only with their original operating conditions.

Ash and impurity interaction, particularly when solid fuel is fired directly in the calciner, can accelerate sorbent deactivation. Sulphation consumes active CaO and can also alter attrition behaviour, so sulphur loading and fuel-ash chemistry must be treated as coupled sorbent-management constraints [31,32].

Reactivation and stabilization strategies include hydration, mechanical treatment and the incorporation of supporting or dopant phases. Their chemical benefits must be evaluated together with particle-size distribution, envelope density, strength, and fluidizability. Steam effects depend on whether it is present during carbonation or calcination and on the exposure history [33].

Recent sorbent studies have investigated calcium aluminosilicates, Mg-, Al-, and Zr-assisted formulations, and combined mechanical and chemical reactivation [34–36]. These studies support continued materials development, but their cycle tests and material preparations differ. Capacity-retention values should be compared only after accounting for temperature, gas composition, conversion basis, and test protocol.

For a bubbling reactor, capacity retention alone is an incomplete sorbent-selection metric. Promising materials should also be reported after pelletisation or granulation with particle-size distribution, apparent density, sphericity, U_{mf}, attrition index, and agglomeration tendency at process temperature. Without those measurements, a high-capacity powder can improve the supply ceiling while simultaneously lowering the hydrodynamic ceiling.

2.4. The Dynamic Geldart Trajectory

The numerical trajectory in Table 2 is an idealised constant-envelope calculation for initially nonporous, pure calcite. With one mole of Ca retained in the particle, carbonation adds CO_2 mass while the envelope volume is fixed at the initial $CaCO_3$ molar volume. The apparent particle density and internal porosity then follow from mass and solid-volume balances. This construction excludes envelope shrinkage or expansion, fragmentation, impurities, and pore coarsening; it is not a universal property law for cycled limestone.

Table 2. Model-derived apparent particle density, intraparticle porosity and minimum fluidization velocity under the constant-envelope assumption; none of these entries is a direct measurement.

X	ρ_{env} (kg·m^{-3})	ε_p	U_{mf} (m·s^{-1})
0.00	1520	0.542	0.02135
0.10	1639	0.488	0.02302
0.20	1758	0.434	0.02470
0.50	2116	0.271	0.02972

Calculations using Wen and Yu [37] employ d_p = 300 μm, $\mu = 3.8 \times 10^{-5}$ Pa·s, and ρ_g = 0.38 kg·m^{-3} at 650 °C. Density and porosity are obtained from ideal stoichiometric volume balances, not measured for a particular limestone.

Skeletal density excludes intraparticle pores; envelope density includes them; bed bulk density also includes interparticle voidage. In the ideal pure-calcite construction, $\rho_{env} = \frac{M_{CaO}+XM_{CO_2}}{V_{CaCO_3}\alpha^3}$, $d_p = d_{p,0}\alpha$, and $\varepsilon_p = 1 - \frac{(1-X)V_{CaO}+XV_{CaCO_3}}{V_{CaCO_3}\alpha^3}$. The molar volumes are 16.9 and 36.9 cm^3·mol^{-1}. The baseline has α = 1; α = 0.9 and 1.1 are selected sensitivities, with unphysical negative porosity excluded.

At U_0 = 0.5 m·s^{-1}, X increasing from 0 to 0.5 raises calculated U_{mf} from 0.02135 to 0.02972 m·s^{-1}. At z = 0.5 m, the associated Darton bubble diameter changes from 0.1556 to 0.1545 m and K_{be} from 0.638 to 0.671 s^{-1}. The integrated 1 m bubble-route depletion changes from 66.3% to 68.4%. Thus a substantial relative density change need not produce a similarly large capture change far above incipient fluidization. The diameter scenarios conserve particle Ca mass and do not model fragmentation losses.

Three levels of evidence should be distinguished: measured changes in sorbent properties and fluidization; derived properties that depend on volume or packing assumptions; and the propagation of those properties through bubble-growth and exchange correlations.

Within-cycle drift is physically plausible, but the percentage density changes in Table 2 are calculated. Direct evidence is stronger for the direction of fluidization change than for this particular density trajectory: Tregambi et al. [38] measured minimum fluidization velocity after individual calcination and carbonation steps at process temperature and found distinct state- and cycle-dependent behaviour. These TCES measurements should not be transferred quantitatively to a 650 °C flue-gas carbonator without matching gas properties, particle history and size distribution.

A continuous carbonator contains a distribution of particle size, carbonation conversion and cycle number. A population balance can represent this joint distribution, with reaction and sintering changing particle properties and with make-up, withdrawal, attrition and elutriation supplying the source and loss terms. A single representative density may suffice when the distribution is narrow; otherwise a size–conversion or size–age discretisation is needed to test segregation and unequal residence times. Results for inert binary mixtures motivate this test but do not establish its magnitude in a reactive CaL bed.

Di Lauro et al. [39] measured particle-size distributions, porosimetry and poured bulk density during fluidized-bed cycling. Their bulk-density measurement includes voids between particles and therefore cannot be substituted directly for the envelope density required in drag or minimum-fluidization calculations. Changes in fragmentation and packing also contribute. These observations support evolving material properties while leaving the constant-envelope magnitudes in Table 2 unvalidated.

Attrition shifts part of the size distribution toward smaller particles, while carbonation, calcination and sintering change density, pore structure and mechanical strength. The resulting movement on a Geldart map need not be monotonic or identical for all particles. Any proposed crossing of the A/B boundary is a hypothesis to be checked against measured size–density distributions and hot-fluidization behaviour; the cold Geldart classification alone does not account for temperature-dependent cohesion.

Figure 3 shows the calculated particle-property sensitivity for a fixed-envelope baseline and two chosen diameter scenarios. No empirical Geldart-group boundaries or measured long-term trajectories are implied. Propagation through U_{mf}, bubble size, and exchange is evaluated under one explicitly defined operating condition.

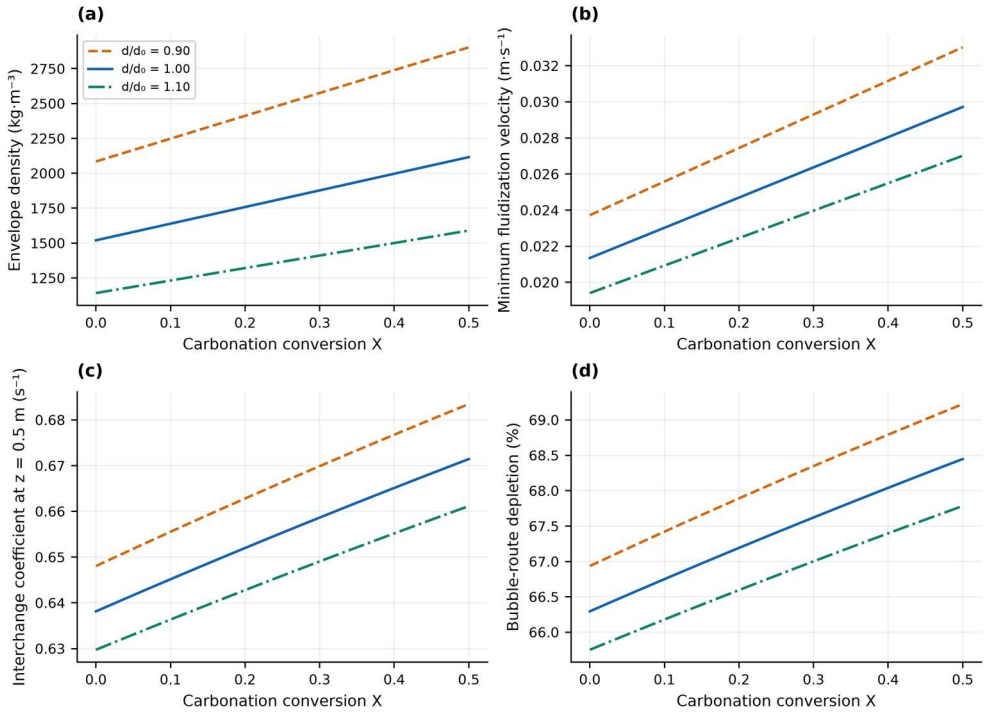


Figure 3. Calculated properties versus carbonation conversion: (**a**) envelope density; (**b**) minimum fluidization velocity using Wen and Yu [37]; (**c**) interchange coefficient at $z = 0.5$ m; (**d**) axially integrated bubble-route depletion over $H = 1$ m. The fixed-envelope

baseline uses d_0 = 300 μm; d/d_0 = 0.90 and 1.10 are mass-conserving sensitivity scenarios, not experimental uncertainty. T = 650 °C and U_0 = 0.5 m·s^{-1}. Diameter and density changes are linked by retained Ca mass; no measured particle trajectory is implied.

3. Hydrodynamics of Geldart B CaO Beds

3.1. Minimum Fluidization at High Temperature

Minimum fluidization provides an input to many bubble correlations. Heating changes gas viscosity and density, while particle cohesion, morphology, and wall friction can also change. In the viscous limit, a fixed noncohesive particle population gives U_{mf} proportional to $d_p^2(\rho_p - \rho_g)/\mu$; the full Wen–Yu relation should be used when the inertial contribution is appreciable. A fixed numerical crossover should not be applied to all hot limestone beds.

Microfluidization measurements on two Geldart B limestones extend direct limestone evidence to 800 °C: U_{mf} decreased with temperature, bubbling began at a lower superficial velocity at 600 °C than at 400 °C, and confinement increased the pressure-drop overshoot [28]. These observations highlight the combined roles of gas properties, particle interactions, and wall effects in small hot beds.

For CaL the practical guidance is:

Determine U_{mf} for the actual hot sorbent where possible. Wen–Yu estimates are useful for sensitivity analysis, but a value obtained with a specified 300 μm particle diameter, density, and gas composition is an example rather than a general property of CaO.

Report the particle-size distribution and the averaging convention. Broad distributions, fines, segregation, and changes in sphericity can alter fluidization relative to a monodisperse calculation; the sign and magnitude of the bias are not universal.

Treat temperature-dependent cohesion and changes in voidage as possible departures from gas-property-only correlations. Their significance should be established from pressure-drop and expansion measurements for the material under study.

3.2. Bubble Formation, Growth and Coalescence

Growth correlations. Three families dominate. Darton et al. [40] treat growth as the result of successive coalescences within a hierarchical catchment structure:

$$d_b = \frac{0.54(U_0 - U_{mf})^{0.4}(z + 4\sqrt{A_0})^{0.8}}{g^{0.2}}$$

Mori and Wen [41] describe an approach to a cross-section-dependent bubble size. Werther-type closures use a different empirical growth dependence for Group B conditions. Figure 4 compares Darton, Mori–Wen, and Werther growth with a common initial diameter of 2 cm, obtained by explicitly shifting the virtual origin of the Darton and Werther relations. The supplementary comparison also retains each correlation's native distributor assumption. These are correlation scenarios; none is newly validated for a hot reacting CaO bed [42–44].

Table 3 retains the Darton calculation as a transparent baseline. Figure 4 adds a correlation comparison and sensitivity to the rise-velocity and interchange closures, so that the numerical implications of selecting one model are visible.

Table 3. Bubble diameter (cm) from the Darton correlation at 650 °C, U_{mf} = 0.0225 m·s^{-1}.

Distributor	U_0 (m·s^{-1})	z = 0.1 m	0.3 m	0.5 m	1.0 m	2.0 m
10,000 orifices m^{-2}	0.3	4.2	8.6	12.5	21.1	36.2
10,000 orifices m^{-2}	0.5	5.3	10.7	15.5	26.3	45.0
10,000 orifices m^{-2}	1.0	7.0	14.3	20.7	35.0	60.0
100 orifices m^{-2}	0.5	14.6	19.1	23.4	33.3	51.3

The unrestricted Darton expression predicts increasing bubble size with elevation, but it has no explicit column-diameter limit. Extrapolating it through a deep vessel or a tube bank can therefore be misleading. Distributor effects enter through the initial catchment area and can persist by influencing emulsion flow and bubble formation; the calculation does not establish a universal height above which distributor design is irrelevant.

Rise velocity is estimated with the Davidson–Harrison form, $u_b = (U_0 - U_{mf}) + \sqrt[0.711]{g d_b}$ [45]. The coefficient and the effect of confinement are model choices. The sensitivity calculation varies this closure explicitly; the assumed range should not be read as a validated error distribution for a reacting CaO bed.

Group-B-specific observations. Optical-fibre measurements in a pilot-scale 3*D* bubbling bed of Group B particles report bubble chord lengths of ~45 mm, approximately three times those observed for Group A under comparable conditions, with bubble frequency below 1.7 Hz and higher in the core than near the wall; the bubble-phase volume fraction remained below 0.5 with the emulsion dominating [46]. Bubble frequency was higher near the distributor than higher in the bed, consistent with coalescence reducing count while increasing size. Force-balance analysis in the same work indicates that agglomeration is intrinsically less likely for Group B than for Group A, which is reassuring for CaL provided the particles remain in Group B, and provides the counterpoint to the concerns of Section 2.4.

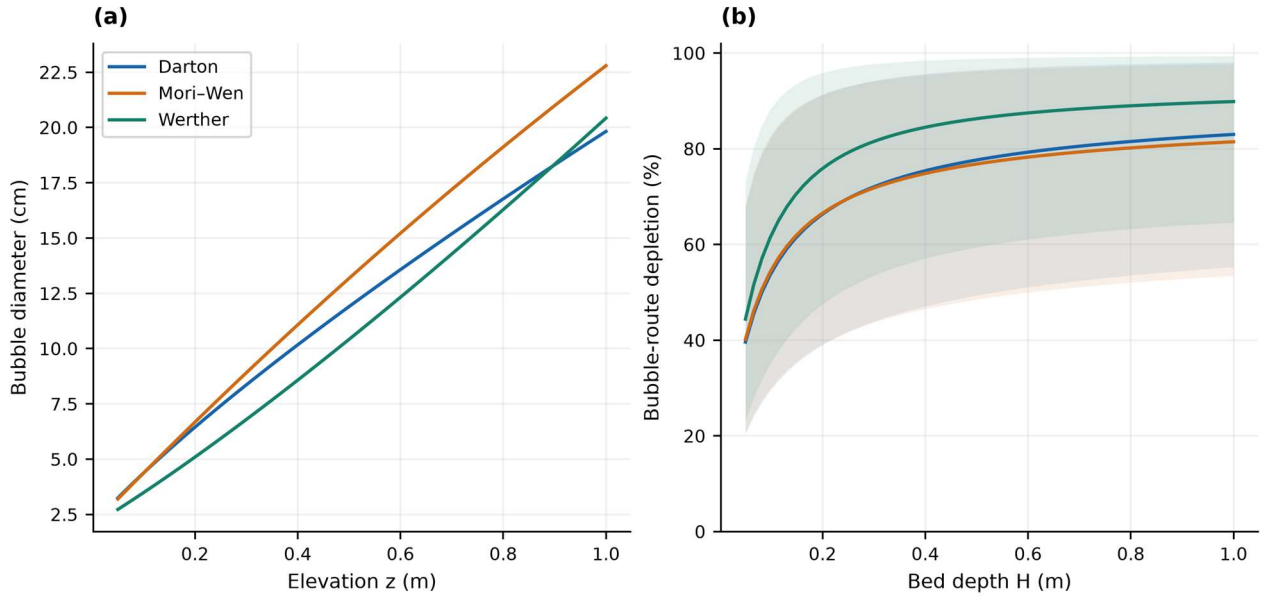


Figure 4. (**a**) Bubble growth and (**b**) integrated bubble-route depletion for Darton et al. [40], Mori and Wen [41], and Werther [42] closures, the latter implemented as reproduced by Jaiswal et al. [43]. Growth is normalized to an initial bubble diameter of 2 cm. U_0 = 0.25 m·s^{-1}, U_{mf} = 0.0225 m·s^{-1}, column diameter = 1 m and T = 650 °C. Shading combines K_{be} multipliers of 0.5–2 and rise-velocity multipliers of 0.85–1.15; these are scenario envelopes, not confidence intervals. Native-distributor results and normalization equations are supplied separately.

Binary-mixture experiments show that composition can modify bubble size and rise velocity [47]. Such results motivate a population description for CaL but do not establish that a reacting, polydisperse CaO/$CaCO_3$ population has systematically smaller bubbles than a corresponding single-component bed.

Pressure changes gas properties, equilibrium, and the fluidization regime simultaneously. It may be a useful design variable, but the atmospheric closures used in the present examples do not establish a quantitative advantage for pressurized CaL. A pressurized design requires appropriate bubble, exchange and kinetic data as well as compression and regeneration balances.

Active bubble control offers an additional design lever. Oscillatory gas flow has been mapped experimentally for 238 micrometre Geldart-B particles and can impose repeatable bubble size, separation

and vertically organised bubble paths within a defined operating window [48]. This does not yet constitute CaL validation, but it shows that bubble diameter need not be treated only as an uncontrolled consequence of bed height and distributor design. Testing oscillatory operation in a hot reacting CaO bed is therefore a credible process-intensification route.

3.3. Measurement: What Can Actually Be Seen in a Hot Reacting Bed

Measurements must resolve transport under the actual thermal and reactive conditions. A central challenge is combining local bubble information with gas composition, solids conversion, and heat flux in one experiment, while quantifying probe and inverse-model uncertainties.

Hot dense-bed diagnostics provide useful measurement methods. Molignano et al. [8,9] resolved local voidage and emulsion expansion with capacitance probes; the 2025 study also used catalytic CO oxidation to assess particle mass transfer. Xie et al. [49] investigated bubble–emulsion transfer in high-temperature beds, and Jiang et al. [50] developed image-based bubble tracking. These studies inform the proposed diagnostic programme, but their materials, chemistry, and inferred quantities must be distinguished from simultaneous CaL capture and heat-flux validation.

3.4. Numerical Simulation

Historical development. Two-fluid modelling of bubbling beds predates modern CaL simulation: Ding and Gidaspow [51] coupled momentum equations with granular fluctuating-energy closures and compared porosity and bubble behaviour with experiments. Theologos and Markatos [10] subsequently demonstrated three-dimensional coupled flow and heat transfer in FCC risers. Their 1993 model included species balances and cracking reaction, and the 1997 extension incorporated a more detailed reaction scheme and feed vaporization with comparison to industrial operating data [11,12]. Related work coupled flow, heat, and mass transfer in fluidized-bed dryers [52]. These precedents establish the historical methodology; they do not validate its closures for CaO carbonation in Geldart-B bubbling beds.

Discrete-particle and coarse-grained approaches. The parallel development of discrete-particle fluidization included the coupled gas–particle simulations of Tsuji et al. [53] and reacting DEM with energy balances for olefin polymerization [54]. Modern coarse-grained CFD–DEM extends this approach to reacting systems with larger particle populations; Wang and Shen [55], for example, coupled flow, heat/mass transfer, and reaction in biomass bubbling-bed gasification. Reaction-dependent density is also represented in multi-fluid models [19]. Coarse-graining reduces computational cost but requires checking that hydrodynamic and thermal/reaction similarity survive the parcel mapping. Particle-wall contact, drag, heat transfer, kinetics, and evolving particle properties remain application-dependent closure choices.

CaL-specific application and validation. Reduced-order bubble/emulsion models and modern CFD provide complementary levels of description. Existing CaL models already combine hydrodynamic and reaction submodels; Guo et al. [18] also studied carbonation with immersed-tube heat transfer. Accordingly, the need is not to introduce coupling for the first time, but to assess which closures are adequate for the target reactor, whether reaction-dependent gas flow and sorbent properties are represented, and which quantities have been validated. A two-dimensional calculation can be useful for its intended geometry and validation target, while unrestricted three-dimensional bubble development requires appropriate three-dimensional treatment. Bulk conversion agreement alone does not establish simultaneous accuracy of bubble statistics, interphase exchange and local bed-to-surface heat transfer.

Recent grain-to-reactor simulations further narrow the modelling gap. Song et al. [56] coupled particle-scale carbonation and heat/mass transfer to CFD–DEM and compared them with published kinetic and thermal data; Song et al. [57] extended this approach to vibration-controlled bubbling. These numerical studies show that explicit bubble–reaction coupling is already available. Their confined quasi-three-

dimensional domains, however, do not establish predictive performance for an unconstrained industrial BFB. The research need is consequently integrated validation over relevant particle histories, tube-bank geometries and operating ranges, rather than the first formulation of reactive coupling.

3.5. Reaction-Induced Hydrodynamic Feedbacks

Reaction and particle evolution create additional feedbacks that should be included when their magnitudes are significant. The following mechanisms are relevant to CaL, although analogous effects occur in other reacting fluidized systems.

(i) Reactive gas contraction in the carbonator. Carbonation removes CO_2 without generating a gaseous product. For 15 vol % inlet CO_2 and 90% capture, total molar gas flow decreases by 13.5%. Superficial velocity falls by the same fraction at constant temperature, pressure, and cross-sectional area. Gas contraction therefore reduces excess gas velocity with height, while coalescence can increase bubble size. Their combined effect belongs in the axial gas and bubble-growth balances; the relative importance depends on inlet CO_2 concentration and capture.

(ii) Gas generation in the calciner. Calcination of 1 kg of pure $CaCO_3$ releases approximately 10 mol of CO_2, equivalent to about 0.96 m^3 at 900 °C and 1 atm. Gas is generated throughout the reacting solids, so superficial velocity and nucleation need not be described by a distributor-only correlation. The stability and magnitude of this effect depend on the imposed fluidization flow, spatial reaction rate, and inventory.

(iii) Sorbent contacting bubble gas. Particle raining, wakes and through-flow complicate the ideal solids-free bubble representation. Their effects can be absorbed only approximately into an effective interchange coefficient. This is one reason the calculations below are conditional transport screens rather than universal upper bounds on real-bed performance.

(iv) Cohesion and agglomeration. High-temperature behaviour depends on sintering, impurities, contact history and particle strength. A Tammann-temperature argument alone is insufficient to establish resistance to defluidization. Measurements of pressure-drop hysteresis, expansion, attrition and particle morphology should accompany hot-bed operation, particularly in the calciner and for fine or synthetic sorbents.

3.6. Summary of Hydrodynamic Gaps

Need for simultaneous bubble statistics, gas conversion, solids conversion and surface heat flux in the same reacting CaO bed, with the operating range stated explicitly.

Need to assess bubble-growth closures when gas is generated or consumed within the bed, rather than assume distributor-anchored inert-bed correlations remain accurate.

Need to test how conversion, particle size, porosity, and cycle history enter hydrodynamic closures; variable-density reactive models in other applications provide useful precedents.

Need for validation of similarity assumptions over the property and reaction ranges relevant to CaL, building on established fluidized-bed scaling methods.

Need for geometry-specific validation of reactive TFM and CFD–DEM predictions, especially close to immersed surfaces and across changes in scale.

4. Heat Transfer at High Temperature

4.1. Carbonation Heat Release and Energy Balance

The carbonation of CaO releases approximately 178 kJ per mole of CO_2 captured. To see what this means, consider the adiabatic temperature rise of the gas alone. For a flue gas containing 15 vol % CO_2 at 90% capture, with a molar heat capacity of ≈33.4 $J \cdot mol^{-1} \cdot K^{-1}$ at carbonator temperature:

$$\Delta T_{\mathrm{ad}} = \frac{0.15 \times 0.90 \times 178{,}000}{33.4} \approx 720\ \mathrm{K}$$

These gas-only adiabatic estimates illustrate the size of the heat release; they are not predictions of bed temperature. A real carbonator also exchanges sensible heat with circulating solids, immersed surfaces, and its surroundings. Bubbling hydrodynamics do not by definition imply a small net solids circulation rate. The relevant heat-removal routes depend on the actual solids withdrawal and return architecture.

For U_0 = 0.5 m·s^{-1}, 650 °C, 1 atm, 15 vol % inlet CO_2 and 90% capture, the approximate reaction duty is 159 kW per m^2 of reactor cross-section when $|\Delta H_r|$ = 178 kJ·mol^{-1} is used. At fixed gas throughput, this areal duty does not increase merely because the bed becomes deeper; dividing by bed depth gives the volumetric duty. The reaction enthalpy is held constant here for screening.

4.2. Mechanisms and the Packet-Renewal Picture

Bed-to-surface heat transfer in a bubbling bed is conventionally decomposed as

$$h = h_{\mathrm{pc}} + h_{\mathrm{gc}} + h_{\mathrm{r}}$$

The packet-renewal description relates particle-convective heat transfer to the arrival, contact time, and replacement of emulsion at a surface [58]. Bubble passage can promote renewal, but it can also replace dense particle contact with gas. The net coefficient depends on the relative importance of these processes and on tube geometry, particle properties, and temperature.

Packet renewal gives a mechanism by which bubble passages can enhance heat transfer, but it does not imply that h increases monotonically with superficial velocity or bubble diameter. More frequent renewal competes with reduced solids contact, increased local voidage, cohesion, and changes in bubble residence at the surface. Accordingly, the sign of the heat-transfer response must be established for the particle material, temperature, surface orientation and tube arrangement under consideration.

Established bed-to-surface correlations provide useful starting points [59–63]. Their particle, surface, and temperature ranges must be checked before use in CaL. A hydrodynamic scaling relation such as Glicksman [64] is not itself a bed-to-surface heat-transfer closure.

4.3. Radiation and the Conditions of Heat-Transfer Measurements

Reported radiative fractions must be interpreted with the experimental temperature, particle material, surface emissivity, and radiation model. Differences among these conditions are not evidence of an intrinsic contradiction between studies.

Table 4 should be read as a comparison of different experiments and modelling assumptions, not as a measured uncertainty interval for CaO. In particular, a radiative fraction observed at 1500 °C must not be used as an estimate for 700–950 °C. For design screening, the total measured or selected coefficient and the separate radiation estimate should be reported with their material, geometry, and temperature basis.

Table 4. Reported radiative contribution to bed-to-surface heat transfer at high temperature.

Source	Conditions	Reported Radiative Contribution
Yoshida et al. [65], experimental	Up to 1000 °C	Insignificant up to 1000 °C
Stenberg et al. [66], experimental, horizontal tube	400–950 °C, d_p 123–327 µm, sand/ilmenite/slag	Convective contribution significantly exceeds radiative; h = 768–1858 W·m^{-2}·K^{-1} at U_0 = 0.15 m·s^{-1}
Chen et al. [67], experimental, vertical surface	300–1500 °C, Al_2O_3/ZrO_2/MgO	<18% below 1200 °C; up to 30% at 1500 °C; smaller particles → higher h but lower radiative fraction

For CaL, the following material and process dependencies merit explicit treatment.

Particle composition and surface condition can change during carbonation and calcination. Radiative properties measured for a separate inert material should not be assigned unchanged to $CaO/CaCO_3$.

Sintering and morphology changes can alter optical behaviour as well as accessible reaction area. Their influence on the radiative contribution requires measurement or a stated constitutive model.

In directly irradiated solar calciners the radiative term is the energy input, not a correction. A validated volumetric energy balance for open and closed directly irradiated bubbling receivers identifies bed-surface emissivity as a critical parameter and reproduced steady-state temperatures with an average absolute relative error of about 5.2% [3]. Limestone/SiC mixtures improve solar absorption but can also modify sorbent deactivation, fragmentation, and segregation, so optical enhancement and fluidization performance must be evaluated together [39].

Stenberg et al. [66] found that heat transfer to a small horizontal tube in inert beds at 400–950 °C increased with superficial velocity only up to a certain value. By contrast, Chen et al. [67], using an immersed vertical surface and oxide particles, reported decreasing h with increasing velocity below 1200 °C. In the latter study, the estimated radiative fraction was below 18% up to 1200 °C and reached approximately 30% at 1500 °C. These results demonstrate condition-dependent behaviour; they do not establish a universal velocity trend or radiative fraction for reacting CaO.

4.4. Thermal Management of the Bubbling Carbonator: A Worked Design Case

The baseline areal reaction duty at 650 °C, 1 atm, $U_0 = 0.5\ m \cdot s^{-1}$, 15 vol % CO_2 and 90% capture is approximately $159\ kW \cdot m^{-2}$. Table 5 gives the required surface density if a 1 m bed removes this entire duty through immersed surfaces. The separate 0.4 m-deep example below includes gas and solids sensible heat and an explicitly specified tube bank.

Table 5. Surface density required for $q''' = 159\ kW \cdot m^{-3}$ if immersed surfaces remove the entire reaction duty. Values are selected h and ΔT scenarios and have units $m^2 \cdot m^{-3}$.

h ($W \cdot m^{-2} \cdot K^{-1}$)	$\Delta T = 50$ K	$\Delta T = 100$ K	$\Delta T = 200$ K
300	10.6 $m^2 \cdot m^{-3}$	5.3 $m^2 \cdot m^{-3}$	2.6 $m^2 \cdot m^{-3}$
500	6.3 $m^2 \cdot m^{-3}$	3.2 $m^2 \cdot m^{-3}$	1.6 $m^2 \cdot m^{-3}$
800	4.0 $m^2 \cdot m^{-3}$	2.0 $m^2 \cdot m^{-3}$	1.0 $m^2 \cdot m^{-3}$

Area density alone is insufficient to demonstrate an operable exchanger. The worked layout below specifies tube diameter, pitch, rows, and occupied volume, and compares the available surface with the heat duty. The selected coefficients and temperature differences are design scenarios, not measurements for this proposed bed.

Tubes change the hydrodynamics on which their own performance depends. Reactive TFM simulation of CaL energy release shows that immersed tubes improve temperature control and reshape solids renewal [18]. A newer Geldart-B tube-bank simulation identifies non-monotonic effects of tube spacing and a velocity-dependent reversal between inline and staggered layouts [68]. The tube bank must therefore be co-designed as heat-transfer area, bubble breaker, pressure-drop element and attrition surface rather than sized after the reactor hydrodynamics have been fixed.

The tube bank must also be assessed for erosion, sorbent attrition, access for maintenance and solids circulation. Geometric feasibility does not establish acceptable service life or freedom from stagnant regions.

Local carbonation heats the bed and raises the equilibrium CO_2 pressure, reducing the local driving force. This negative reaction feedback can lower capture even when the global heat balance appears adequate. It does not replace a transient thermal-safety assessment. The coupled calculation in Section 6 illustrates the performance effect at an assumed uniform bed temperature.

Guo et al. [18] numerically predicted that increasing inlet CO_2 concentration could increase carbonation while reducing particle renewal and the heat-transfer coefficient in a BFB energy-release reactor. This is a model-based coupling mechanism, not a direct experimental observation. Simultaneous local solids-contact and heat-flux measurements in a reacting CaL bed are needed to test it.

A realizable illustrative layout has a 1 m × 1 m plan area and 0.4 m expanded bed depth, with 20 horizontal tubes of 25 mm outside diameter and 1 m immersed length. Two rows of ten tubes use 95 mm horizontal and 160 mm vertical pitch, with row centres 100 and 260 mm above the distributor. The surface area is 1.571 m^2, or 3.93 $m^2 \cdot m^{-3}$, and tubes occupy 2.45% of the bed volume. Figure S1 shows the geometry. Headers, supports, expansion allowances, and steam-side constraints require subsequent design.

Using constant approximate $|\Delta H_r|$ = 178 $kJ \cdot mol^{-1}$ at bed temperature, gas heat capacity 33.4 $J \cdot mol^{-1} \cdot K^{-1}$, and solids heat capacity 1.0 $kJ \cdot kg^{-1} \cdot K^{-1}$, the reaction duty is 158.6 kW. The inlet gas at 600 °C supplies a sensible-heat sink of 11.0 kW, evaluated on inlet flow. With return solids at 625 °C, their sensible sink is 10.4 kW and the surfaces must remove 137.2 kW. Return solids at 850 °C instead add 83.3 kW, increasing the surface duty to 230.9 kW. Wall losses are omitted.

For h = 500 $W \cdot m^{-2} \cdot K^{-1}$ and a mean tube-wall temperature of 350 °C, the bank capacity is 235.6 kW. Required bed-to-wall temperature differences are 175 and 294 K for the two return scenarios. The hot-return case has little margin; at h = 300 $W \cdot m^{-2} \cdot K^{-1}$ it is infeasible. This is a feasibility calculation, not validation of h, acceptable erosion, bubble breakup or local temperature uniformity.

4.5. Heat Transfer in the Calciner

Calcination requires heat at conditions that depend on CO_2 partial pressure and the desired rate. Oxy-fuel firing, indirect heating and concentrated solar irradiation impose different boundary conditions, gas-generation profiles and material constraints.

Oxy-fuel calcination has been demonstrated in MW-scale CaL pilots [1,2]. Indirect heating separates the solids from combustion products but requires an adequate area and temperature difference. Solar designs add an incident-radiation boundary condition and depend on surface renewal and optical absorption [3]. These examples should be distinguished from experimental validation of a complete bubbling carbonator–calciner design.

4.6. Heat Transfer Gaps

Quantify radiative and convective contributions for the relevant sorbent, temperature, and surface geometry instead of assigning a single generic radiative fraction.

Measure effective optical properties over conversion and cycle history using a stated wavelength range and temperature protocol.

Expand measurements of local and mean surface heat transfer in reacting CaL beds, including uncertainty and heat-balance closure.

Validate or recalibrate correlations over the intended range of particle properties, velocity, and tube arrangement.

Measure the joint effects of tube banks on bubble transport, solids renewal, heat transfer and capture; numerical studies provide hypotheses to test.

5. CO_2 Capture Performance in the Bubbling Regime

5.1. Reactor Models

Carbonator models already connect gas–solid contact with reaction and sorbent management [69]. Shimizu et al. [15] treated a BFB absorber and its heat-recovery requirements; Romano [16] developed a K–

L-based CFB model; and Charitos et al. [17] tested an active-space-time description against two CFB facilities. The active-space-time representation remains useful for organising inventory and reaction capacity:

The inventory description builds on established capacity and conversion-limit studies [70,71]. A model comparison in Supplementary Table S1 includes Shimizu et al. [15], Lasheras et al. [72], Romano [16], Charitos et al. [17], Diego et al. [73], Ylätalo et al. [74] and Hornberger et al. [22]. Hawthorne et al. [75] and their subsequent carbonator work is represented by the verified coauthored experimental and modelling studies in that comparison.

$$\tau_{\mathrm{act}} = \frac{n_{\mathrm{Ca}}\, f_{\mathrm{a}}}{F_{\mathrm{CO_2}}}$$

Here n_{Ca} is the total molar inventory of Ca and f_{a} is the fraction assigned to the selected active reaction regime. Both depend on particle residence-time and cycle-history distributions. The formulation therefore links inventory, circulation and sorbent behaviour rather than making them independent. A separate stoichiometric screening condition follows from the Ca balance:

$$E_{\mathrm{supply}} = \min\left[1, \frac{F_R \Delta X_{\max}}{F_{\mathrm{CO_2,in}}}\right]$$

The relation is a capacity balance, with F_{R} expressed as moles of circulating calcium per second and ΔX as the achieved conversion increment per pass. For 90% capture, ΔX = 0.10–0.15 requires Ca/C = $F_{\mathrm{R}}/F_{\mathrm{CO2}}$ of at least 9–6, respectively. A range of 4–10 therefore spans different supply limits and cannot be called a general high-capture recommendation. Section 6 shows the resulting binding-constraint map.

A continuous BFB concept requires controlled dense-phase withdrawal or overflow to a standpipe/loop seal or solids valve, transfer to the calciner, and an imposed return of regenerated sorbent. Hornberger et al. [22] provide experimental precedent for a BFB carbonator connected to a CFB calciner. The present example is not a scaled reproduction of that pilot. Staged beds additionally require specified solids allocation and gas redistribution between stages.

For the 0.4 m-deep example in Section 4.4, Ca/C = 7.5 gives F_{R} = 7.426 mol·Ca·s^{-1}, equivalent to 0.416 kg·s^{-1} CaO return. A 90% capture target requires ΔX = 0.12. Assuming X_{in} = 0, well-mixed X_{out} = 0.12, bubble hold-up 0.35, and emulsion voidage 0.50, the tube-corrected inventory is 210.9 kg or 3437 mol Ca. Its turnover $n_{\mathrm{Ca}}/F_{\mathrm{R}}$ is 463 s (7.7 min). This finite circulation rate must be provided by the solids loop.

With a selected make-up ratio $F_0/F_{\mathrm{CO2,in}}$ = 0.05 and equal-probability well-mixed purge, F_0/F_{R} = 0.00667 and the ideal mean number of passes before purge is 150. This does not ensure ΔX = 0.12: a cycle-age/size population balance must account for deactivation, make-up, attrition, elutriation, and unequal residence times. If the achievable increment is smaller, the stated 90% target fails the supply constraint.

Tizfahm et al. [30] tested carbonation kinetics against laboratory data and incorporated them into a one-dimensional model with fast-fluidization hydrodynamics. This is useful carbonator modelling evidence, but validation of the kinetic submodel does not establish a bubbling-bed hydrodynamic closure.

Reduced-order models need not resolve individual bubbles to be useful, provided their exchange and mixing closures are appropriate and independently tested for the regime and geometry. A CFB dense/lean-zone closure should not be transferred unchanged to a shallow BFB with immersed tubes. Conversely, a BFB bubble–emulsion calculation is an interpretation of transport sensitivity, not evidence that established CFB models fail.

5.2. Evidence from Bubbling and Related Fluidized Systems

The evidence spans reacting CaL experiments, inert Group B beds, other reacting systems and numerical models. The comparison below identifies the evidence class and the limit of transfer to a CaL bubbling bed. Particle conversion, cyclic capacity retention, and inlet-to-outlet CO_2 capture are distinct quantities and are not compared as interchangeable performance measures.

Cyclic capacity loss is well established, but the rate depends on precursor and cycling conditions [29]. In fluidized CaL-TCES experiments, Di Lauro et al. [39] measured conversion, bulk density, and fragmentation over repeated cycles. These measurements support an evolving particle population without proving a universal envelope-density trajectory.

Steam-assisted carbonation and hydration can improve conversion in some protocols, while regeneration conditions may accelerate sintering or attrition. The chemical and mechanical effects should therefore be evaluated over the complete cycle rather than inferred from carbonation-only tests [32,33].

Modified sorbents illustrate the need to report the reaction and hydrodynamic bases together. Capacity retained in a laboratory cycling test is not equivalent to capture efficiency in a continuously fed bubbling reactor. The review therefore avoids using sorbent-screening percentages as evidence for a reactor-level capture ceiling.

Fine or assisted-fluidization powders can be relevant to adjacent CaL applications, but results outside the conventional Group B regime should not be transferred directly to the present screening calculations.

In dual-fluidized-bed configurations incorporating a compact bubbling carbonator, long-term stable operation has been demonstrated and normalised capture-efficiency models developed, with constructional constraints, operating conditions and sorbent characteristics all exerting strong effects on capture efficiency and active space time [5].

Directly irradiated beds also involve coupled optical, thermal, and particle-evolution effects. Briongos et al. [3] and Di Lauro et al. [39] inform different parts of this problem; neither alone establishes the capture performance of an internally cooled post-combustion carbonator.

Moghtaderi and Seyfaee [76] compared instrument-, bench-, laboratory-, and pilot-scale equipment and found nonlinear scale dependence, which they attributed to differing heat- and mass-transfer limitations. Their results support explicit transport assessment when moving between scales.

At low CO_2 concentrations, fluidized-bed measurements show that the same experiment can move from intrinsic kinetic control to external mass-transfer control as temperature and driving force change. This provides direct experimental support for separating the kinetic/supply and hydrodynamic ceilings instead of fitting a single apparent rate constant [25].

Taken together, these studies support coupling material behaviour to reactor transport. They do not establish that every small bubbling bed is free of transport limitations or that hydrodynamic bypass dominates every large one.

5.3. The Bypass Penalty: Quantifying the Hydrodynamic Ceiling

The first calculation isolates bubble–emulsion exchange by assuming a sufficiently reactive emulsion and specified hydrodynamic closures. The quantity $1 - \exp(-N_x)$ describes depletion of the bubble-stream excess concentration in the limiting zero-equilibrium case. It should not be equated automatically with total-reactor CO_2 capture. The calculation distinguishes this exchange metric from a gas-balance-based ideal-bed capture estimate.

$$E_b = 1 - \exp(-N_x), N_x = \int_0^H \frac{K_{be}(z)}{u_b(z)} dz$$

$$E_{h,0} = \frac{U_{mf}}{U_0} + \left(1 - \frac{U_{mf}}{U_0}\right) E_b$$

$E_{h,0}$ is only a zero-equilibrium ideal-two-phase screen, with complete uptake from the emulsion inlet stream. The staged gas-route model in Figure 5 instead updates composition and superficial velocity axially and is described separately in the Supplementary Information. These different limiting constructions must not be treated as the same model.

The exchange calculation adopts the bubble–cloud and cloud–emulsion closures described by Kunii and Levenspiel [77,78]:

$$K_{\mathrm{bc}} = 4.5\frac{U_{\mathrm{mf}}}{d_{\mathrm{b}}} + 5.85\frac{D^{1/2}g^{1/4}}{d_{\mathrm{b}}^{5/4}}, \qquad K_{\mathrm{ce}} = 6.77\left(\frac{\varepsilon_{\mathrm{mf}} D\, u_{\mathrm{b}}}{d_{\mathrm{b}}^{3}}\right)^{1/2}, \qquad \frac{1}{K_{\mathrm{be}}} = \frac{1}{K_{\mathrm{bc}}} + \frac{1}{K_{\mathrm{ce}}}$$

Table 6 recomputes the constant-bubble-diameter examples at 650 °C, $U_{\mathrm{mf}} = 0.0225$ m·s^{-1}, $D = 1.2 \times 10^{-4}$ m^2·s^{-1}, $\varepsilon_{\mathrm{mf}} = 0.50$, $U_0 = 0.5$ m·s^{-1} and $H = 1$ m. The reported envelope varies K_{be} by factors 0.5–2 and u_{b} by factors 0.85–1.15, recalculating K_{ce} consistently. No probability distribution is assigned to these factors.

Table 6. Constant-diameter transport diagnostics. E_{b} is bubble-stream depletion under a zero-equilibrium fast sink; $E_{\mathrm{h,0}}$ additionally assumes complete capture of the ideal emulsion inlet flow. Neither is a validated total-reactor prediction at finite equilibrium.

d_{b} (cm)	u_{b} (m·s^{-1})	K_{be} (s^{-1})	E_{b} Baseline	E_{b} Range	$E_{\mathrm{h,0}}$
2	0.79	9.07	100.0%	99.4–100.0%	100.0%
5	0.98	2.76	94.1%	72.2–99.8%	94.4%
10	1.18	1.13	61.6%	35.2–88.2%	63.3%
15	1.34	0.67	39.5%	20.4–67.4%	42.2%
20	1.47	0.47	27.1%	13.4–50.6%	30.4%
30	1.70	0.28	15.2%	7.2–30.7%	19.0%

The strong dependence on bubble diameter is conditional on the assumed depth, flow partition and interchange closure. The range in the table propagates stated changes in exchange and rise velocity; it is not a measured uncertainty interval. Neither sorbent activity nor inventory can be dismissed on the basis of this calculation, since the fast-emulsion assumption already presumes sufficient reaction capacity.

A nonlinear average over bubble sizes differs from evaluation at the mean. For two equally gas-flux-weighted diameters, $\bar{d}(1 - \mathrm{w})$ and $\bar{d}(1 + \mathrm{w})$, calculate $E_{\mathrm{b}} = 1 - \sum_i w_i \exp(-N_{x,i})$. At $\bar{d} = 5$ cm, choosing $\mathrm{w} = 0.5$ lowers E_{b} from 94.1% to 88.9%; at $\bar{d} = 15$ cm it raises E_{b} from 39.5% to 50.4%. These constructed distributions demonstrate that even the sign of the averaging effect is condition dependent. Probe chord lengths, projected diameters and volume-equivalent diameters must be distinguished.

With a common initial bubble diameter of 2 cm, $U_0 = 0.25$ m·s^{-1} and $H = 1$ m, Darton, Mori–Wen and Werther give integrated bubble-route depletions of 83.0%, 81.5% and 89.9%, respectively. Using only the largest, outlet bubble over the entire bed discards the stronger exchange near the distributor and can markedly understate the integrated result. The supplementary native-distributor comparison separates this averaging error from the initial-condition choice.

At fixed bubble size, a greater depth increases the residence time and the number of transfer units. In a freely growing bubble field, both bubble size and transfer coefficient change with elevation. The corresponding axial integral, rather than an outlet bubble diameter applied over the whole bed, is used in the comparison.

Adding bed depth can improve conversion and inventory, but its benefit depends on bubble growth, gas contraction, internals, and the solids residence-time distribution. At fixed feed and capture, a deeper bed does not automatically require a larger total heat-transfer area; its heat-release density is lower. Pressure drop and solids hold-up must be assessed separately.

Potential transport interventions include bubble breakup, improved gas distribution, and staged contact. Each changes more than one part of the reactor balance and requires a geometry-specific evaluation.

Shallow stages with gas redistribution can reduce the height available for coalescence. Figure 5 compares this hypothesis with a single bed and an imposed bubble-size cap representing idealized internals. The calculation specifies the bubble-growth reset and updates interstage composition and flow. Sufficient

active sorbent is assumed; solids routing and allocation remain outside this model. The comparison does not establish an optimum stage depth.

At a total depth of 1 m, 650 °C and inlet U_0 = 0.5 m·s^{-1} with 15% CO_2, the gas-route screen gives 64.6% for one bed, 91.3% for four ideal redistributed stages, and 90.5% or 74.0% with imposed 5 or 10 cm bubble caps. These optimistic comparisons assume sufficient active sorbent and cooling at each location. Their common gas-contact height does not imply equal exchanger occupation or validated solids residence-time distributions.

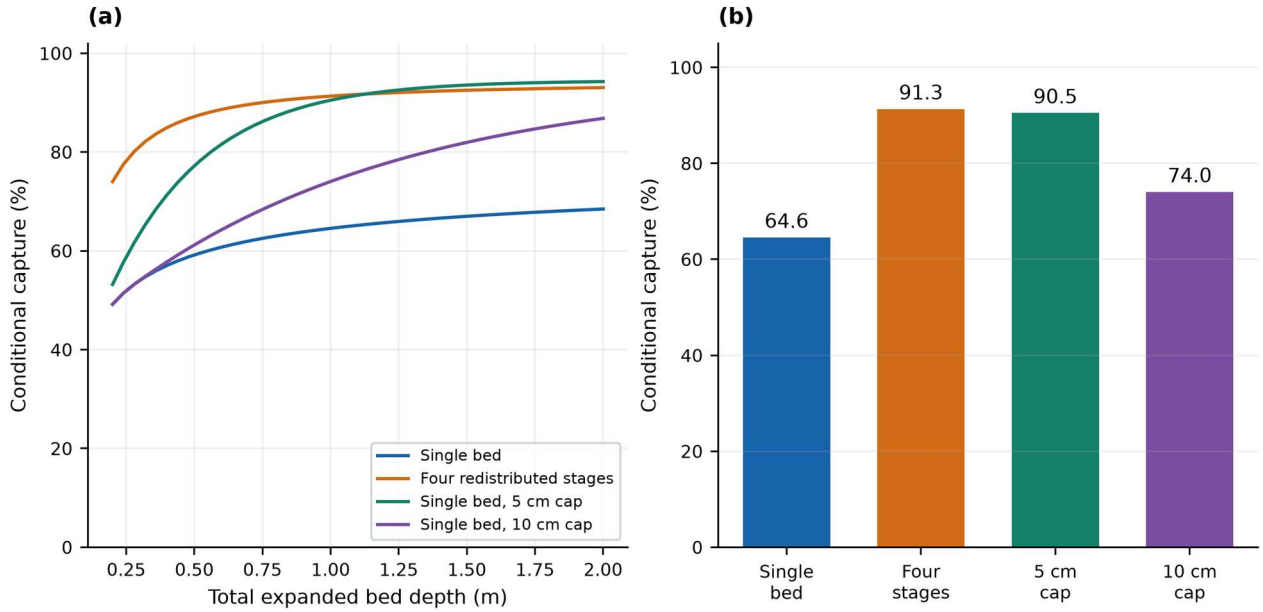


Figure 5. Conditional gas-route capture with evolving bubbles, finite equilibrium and gas contraction: (**a**) variation with total bed depth; (**b**) comparison at a common total depth of 1 m. Cases comprise a single bed, four equal stages with complete gas redistribution, and imposed 5 or 10 cm bubble caps. The Darton-based model uses T = 650 °C, inlet U_0 = 0.5 m·s^{-1} and 15% CO_2. Fast reaction and sufficient active sorbent and heat removal are assumed. Bubble resets and caps are idealized and are not derived from the tube-bank geometry. Finite kinetics, pressure losses and interstage solids allocation are outside this calculation.

The selected exchange closure omits explicit through-flow, bubble solids, and spatial variations in emulsion voidage. Consequently, it may underpredict or overpredict transfer in a particular freely bubbling bed. A conditional fast-sink calculation is an upper limit within its own model assumptions, but is not a rigorous upper bound across alternative real-bed hydrodynamics. Finite kinetics, thermodynamic driving force, and solids supply are treated separately and in the coupled example. Table 7 classifies the supporting measurements and model inferences.

Table 7. Evidence relevant to coupled CaL BFB design. A: reacting CaO BFB measurements; B: inert or nonreacting Group B measurements; C: another reacting fluidized system; D: numerical or conceptual inference. These classes identify provenance, not a universal ranking of study quality.

Study/Class	Configuration	Evidence	Design Implication and Limit
Tregambi et al. [38]/A	CaL-TCES fluidized cycling at 850/950 °C	Hot U_{mf} measured after calcination/carbonation; particle properties tracked.	Supports state-dependent fluidization; does not validate the constant-envelope model at 650 °C.
Di Lauro et al. [39]/A	40 mm BFB; limestone with/without additives; 20 cycles	Conversion, PSD, porosimetry, and poured bulk density.	Evolving particles matter; bulk density includes packing and is not envelope density.
Ooi and Marek [25]/A	30 mm BFB with dilute quicklime samples in silica sand; 400–650 °C	Carbonation kinetics screened against external mass transfer at 0.38–2.70 vol% CO_2.	Useful dilute-condition kinetics; not atmospheric-CO_2 or full-inventory CaO-bed validation.

Hornberger et al. [22]/A	200 kW BFB carbonator–CFB calciner pilot	Capture and active-space-time model under cement-related conditions.	Real circulation architecture; performance and fitted rates remain configuration-specific.
Stenberg et al. [66]/B	Horizontal 6 mm tube; sand, ilmenite and slag at 400–950 °C	Measured bed-to-tube heat-transfer coefficients.	Direct thermal evidence for the tested geometry and materials; not reacting CaL validation.
Molignano et al. [9]/B and C	Group-B bed at ambient/450 °C; catalytic CO oxidation	Capacitance-probe hydrodynamics and particle mass-transfer measurements.	Relevant instrumentation and emulsion-voidage evidence; chemistry is not CaL.
Asiedu-Boateng et al. [28]/B (supporting)	Limestone microfluidization up to 800 °C	Pressure-based fluidization/bubbling/slugging response to temperature and confinement.	Hot-limestone flow evidence; not a controlled carbonation-conversion series.
Guo et al. [18]/D	Reactive CaL-TCES TFM with immersed tubes	Predicted coupled effects of gas composition, velocity, and tube insertion.	Identifies testable feedback mechanisms; h reduction is a prediction.
Guo et al. [68]/D	2D TFM; Group-B bed with horizontal tube bundles	Predicted effects of tube pitch/layout, velocity and particle size.	Geometry-dependent heat transfer; not a 3D reacting-CaL experiment.
Song et al. [56,57]/D	Confined quasi-3D CFD–DEM; grain-to-reactor reaction model	Numerical bubble–reaction coupling and vibrational structuring.	Extends mechanistic modelling; industrial hot-bed closure validation remains separate.

5.4. Conditional Operating Criteria

The operating ranges below are screening choices for the stated examples. Selection for a particular reactor should satisfy the capture target, sorbent turnover, heat balance, stable fluidization, acceptable pressure drop and attrition limits simultaneously. No universal optimum superficial velocity or stage depth is proposed. Table 8 summarizes the resulting operating criteria.

Table 8. Conditional operating criteria for case-specific design.

Variable	Criterion or Stated Example	Required Check
Carbonation T	Selected from equilibrium and measured kinetics	550–600 °C dilute-feed example is not universal
Superficial velocity	Specify U_0/U_{mf} and the actual gas throughput	Stable bubbling, transport, attrition and pressure drop
Particle size	300 µm nominal in the calculations	Measured PSD, density, strength and hot U_{mf}
Stage depth	Compare single bed and redistributed stages	0.25 m stages in Figure 5 are illustrative
Ca/C and ΔX	Ca/C $\geq E_{target}/\Delta X$	90% needs ≥6 at $\Delta X = 0.15$ or ≥9 at 0.10
Make-up	Selected $F_0/F_{CO2} = 0.05$ example	Population balance must support required ΔX
Tube bank	Specified geometry and measured h	Heat balance, bubble modification, erosion and solids flow
Calcination	T and p_{CO2} sufficient for desired conversion rate	Regeneration kinetics, energy duty and sorbent deactivation

5.5. Applications Beyond Post-Combustion Capture

Thermochemical energy storage. BFB operation provides a route to retain reactive solids and exchange heat with immersed surfaces. Fluidized tests show that additives affect deactivation, fragmentation, density and segregation as well as optical properties [39]. The nonlinear scale dependence reported by Moghtaderi and Seyfaee [76] further supports transport-aware design rather than extrapolation from TGA capacity alone.

Dilute-source capture requires explicit equilibrium and gas-delivery checks. Ooi and Marek [25] studied 0.38–2.70 vol % CO_2 in a fluidized bed; their measurements do not directly validate performance

at atmospheric CO_2 concentration. Extrapolation toward air capture should therefore include independently established kinetics and equilibrium at the lower partial pressure.

Sorption-enhanced reforming and gasification. *In-situ* CO_2 removal shifts the water–gas shift and reforming equilibria, and here the bubbling bed's ability to host sorbent, catalyst, and fuel simultaneously is decisive. Compact bubbling carbonators within dual-fluidized-bed systems have been operated under electrically heated hot conditions specifically to develop sorption-enhanced gasification and tar cracking intensification [5].

Cement. The cement industry is both a major CaL application and a natural sink for the purge stream. Recent laboratory fluidized-bed tests using real cement-plant flue gas compared limestone with white-mud-derived CaO and found that moisture and 15 vol % steam improved cyclic capture under the reported conditions, including at a reduced calcination temperature of 910 °C [79]. The result is promising for waste valorisation, but scale-up still requires attrition, impurity accumulation and solids-circulation evidence.

6. The Coupled Picture: A Four-Ceiling Framework

6.1. Statement of the Framework

The four-constraint framework classifies equilibrium, exchange, reaction and supply, and thermal feasibility at the same specified state. The first three can yield conditional capture limits; the thermal condition closes the energy balance and thereby changes the state on which those limits depend. They are not physically independent constraints.

$$E_{\mathrm{screen}} = \min\left(E_{\mathrm{eq}}, E_{\mathrm{h,0}}, E_{\mathrm{rxn/supply}}\right)$$

Taking the minimum provides a screening comparison only when all bounds use consistent temperature, pressure, flow basis, inventory, and closures. It is not a predictive combination rule. An equilibrium bound is thermodynamic, a supply bound is stoichiometric, and a transfer estimate depends on the selected phase model. Thermal feasibility must be checked through an energy balance rather than treated as a universal fourth scalar cap. The crossover calculation below demonstrates the gap between separate limits and a coupled solution. Table 9 defines the diagnostic meaning and limits of the four categories.

Table 9. Meaning and limitations of the four constraint categories.

Category	Diagnostic	Qualification
Equilibrium	E_{eq} on inlet CO_2 molar-flow basis	Thermodynamic limit at stated pressure and temperature
Transport	E_b or $E_{h,0}$ with explicitly stated phase basis	Closure-dependent idealization; real through-flow can differ
Reaction and supply	Finite k_r and min(1, Ca/C × ΔX_{max})	Kinetic coefficient, activity and inventory bases must match
Thermal feasibility	Required surface duty versus available removal	Energy balance changes the temperature of all other constraints

6.2. Binding Constraints and an Illustrative Coupled Calculation

The binding constraint depends on operating conditions and may change with scale. The examples below vary sorbent supply and hydrodynamic assumptions explicitly; scale labels alone are not assigned capture efficiencies.

A small bed can have favourable exchange and a large wall area per unit volume, but short gas residence time, wall effects, slugging and limited solids inventory can still constrain performance. Micro-fluidized-bed results require transport screening before being interpreted as intrinsic kinetics [6,25,28].

Larger vessels permit different bubble structures and usually have a smaller external wall area per unit volume. Tube banks, baffles, gas staging and distributors can alter these trends. Generic capture-efficiency ranges therefore cannot be assigned to pilot or industrial scale without the operating conditions, geometry, and active sorbent inventory.

Thermal constraints likewise depend on concentration, throughput, sensible-heat transport and installed exchanger area. They cannot be inferred from scale alone. A shallow stage may have a high volumetric duty and a short solids turnover time even when its individual gas-contacting characteristics are favourable.

Multiscale CaL-TCES experiments show that responses need not scale linearly between instruments and pilot equipment [76]. Such evidence motivates transport-aware scale-up, but it does not validate the values or ordering of the conditional bounds in this review. Figure 6 therefore evaluates explicit supply and coupled-model sensitivity examples.

The supply scenarios Ca/C = 4–10 and $\Delta X = 0.10$–0.15 span $E_{supply} = 40$–100%. At Ca/C = 4, the supply limit is 40–60%, so hydrodynamics cannot be presumed dominant. Figure 6a,b applies equilibrium and ideal transport screens to the same specified state and marks where supply is more restrictive. These maps exclude a solved heat balance and are not achieved-capture predictions.

A reduced coupled example uses 1 vol % inlet CO_2, $H = 0.5$ m, $U_0 = 0.25$ m·s^{-1}, Ca/C = 7.5, $\Delta X_{max} = 0.12$, $h = 300$ W·m^{-2}·K^{-1} and a = 5 m^2·m^{-3}. Gas, return solids, and mean coolant wall enter at the reference temperature, varied from 550 to 600 °C. The bed is thermally well mixed. An effective total-bed-volume first-order coefficient k_r has selected values 0.1, 0.5, and 2 s^{-1} at 575 °C and an assumed activation energy of 30 kJ·mol^{-1}. These are sensitivity inputs, not measured intrinsic kinetic constants.

The local closure balances transport and reaction through an intermediate concentration C_r:

$$k_m(C_{bulk} - C_r) = k_r(C_r - C_{eq}), k_m = \frac{UK_{be}}{u_b}$$

Eliminating that concentration gives the effective axial coefficient:

$$a_{eff} = \left[\left(\frac{K_{be}}{u_b}\right)^{-1} + \left(\frac{k_r}{U}\right)^{-1}\right]^{-1}$$

The gas-route balance is then written for CO_2 flux F and conserved inert flux I:

$$\frac{dF}{dz} = -a_{eff}\left[F(1 - y_{eq}) - Iy_{eq}\right], U = \frac{(F + I)RT}{P}$$

Cumulative uptake per plan area is capped by $J_R\,\Delta X_{max}$, where $J_R = F_R/A$. The uniform bed temperature simultaneously satisfies:

$$J_{CO_2,in}E|\Delta H_r| = \left[haH + J_{g,in}C_{p,g} + G_{s,in}C_{p,s}\right](T - T_{ref})$$

Here, all J quantities are molar fluxes (mol·m^{-2}·s^{-1}), G_s, in is the solids mass flux (kg·m^{-2}·s^{-1}), and A is the plan area. Reaction enthalpy is held constant at an approximate bed-temperature value. Gas contraction updates U through the local total molar flux.

This is an explicitly defined phenomenological one-route mass/energy surrogate. It couples exchange, finite reaction, equilibrium, gas contraction, and temperature-dependent gas properties but does not resolve separate bubble/emulsion balances, a particle population, or local hot spots. Separate limiting screens remove the competing resistances; their minimum is compared with the coupled solution in Table 10 and Figure 6c. At 575 °C and $k_{r,ref} = 0.5$ s^{-1}, the minimum is 63.3%, the isothermal coupled result is 35.4%, and the thermally coupled result is 35.1% at a bed temperature of 577.5 °C. Most of the gap here arises from simultaneous finite transport and reaction, rather than the small temperature rise.

Table 10. Illustrative reduced coupled results for $k_{r,ref} = 2$ s^{-1}. The separate minimum changes from a transport to an equilibrium screen; the coupled values are unvalidated model calculations.

Reference T (°C)	Minimum Screen	Coupled Capture	Bed T (°C)	Gap (Percentage Points)
550	82.3%	57.1%	554.2	25.2
575	82.9%	54.1%	578.9	28.8
600	73.1%	46.3%	603.3	26.8

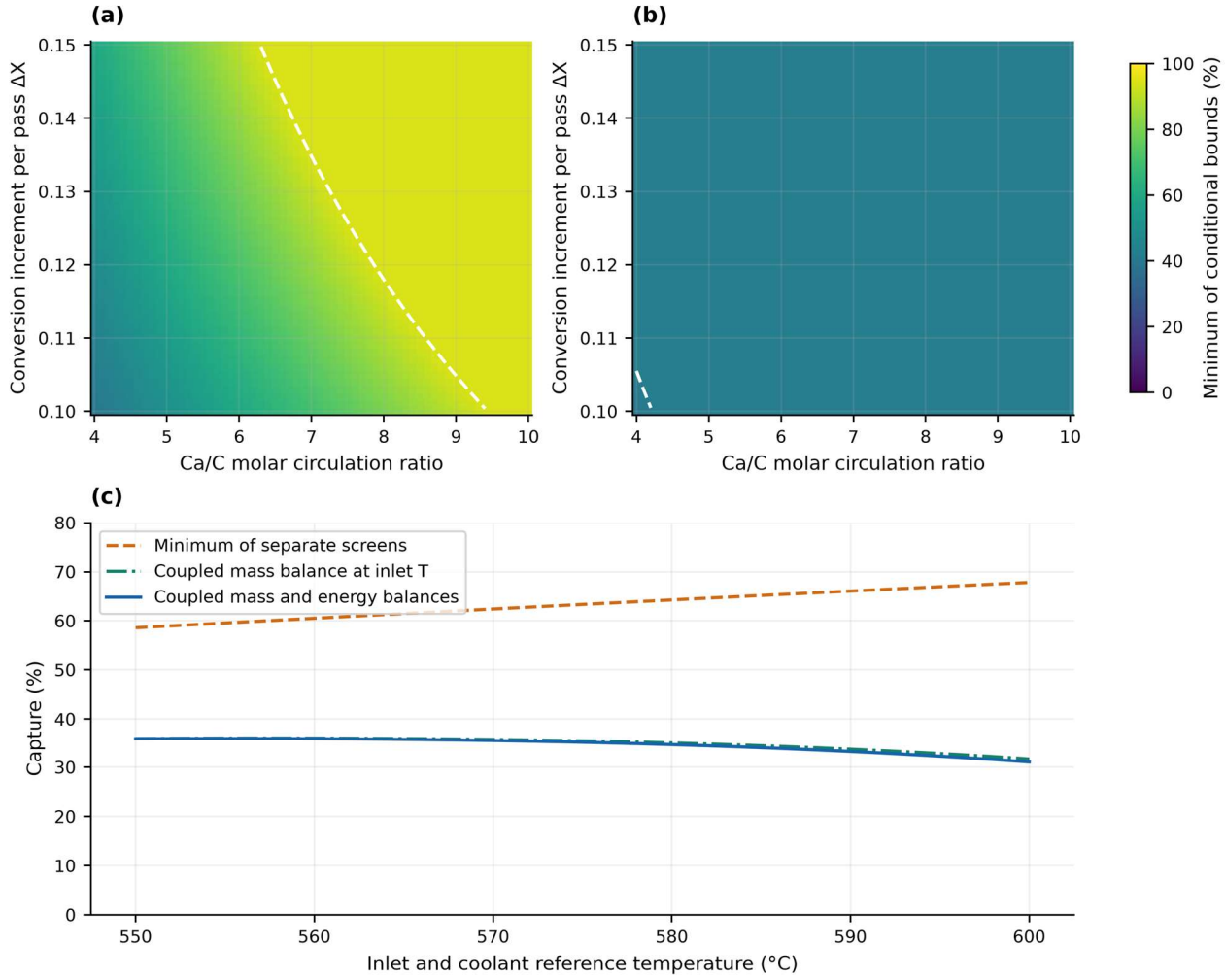


Figure 6. Minimum-screen maps for (**a**) constant 5 cm and (**b**) constant 15 cm bubbles at 650 °C, 15% inlet CO_2, H = 1 m and U_0 = 0.5 m·s^{-1}. The white dashed line separates supply- and transfer-limited screens. (**c**) Separate limiting estimates compared with the reduced coupled mass/energy model for 1% inlet CO_2, H = 0.5 m and U_0 = 0.25 m·s^{-1}. The effective rate coefficient at 575 °C is 0.5 s^{-1}, h = 300 W·m^{-2}·K^{-1} and a = 5 m^2·m^{-3}. All panels are illustrative calculations; the one-route model is not a validated two-phase reactor simulation.

6.3. Velocity and Thermal Design Sensitivity

Changing superficial velocity modifies throughput and several interacting transport mechanisms. In the illustrated constant-property closures, increasing excess velocity has the following conditional effects.

Darton bubble growth increases with excess velocity, while bubble residence time and the predicted exchange integral change with both size and rise velocity.

Gas throughput and reaction duty per unit cross-section increase at fixed temperature, composition and target capture.

Particle renewal at immersed surfaces may increase, saturate, or decrease. The sign must be established for the selected particles, surface geometry and thermal regime.

Attrition, entrainment, pressure drop and transitions out of freely bubbling operation can restrict the feasible velocity range.

An interior optimum may occur for a specified objective and constraints, but it is not guaranteed. The 0.48–0.74 m·s^{-1} interval reported in the simulation of Guo et al. [18] is a result for that configuration and cannot serve as a general CaL design recommendation. The figure uses explicit sensitivity cases without treating their overlap as a validated optimum.

$$\max_{\text{operating conditions, geometry}} E$$

Optimization requires solving the same mass, energy, and solids balances for every candidate geometry and operating condition. Particle properties, distributor, tube arrangement, feed composition, pressure drop and attrition constraints must be specified before an optimum can be assigned. Figure 7 illustrates the selected velocity and heat-transfer sensitivities.

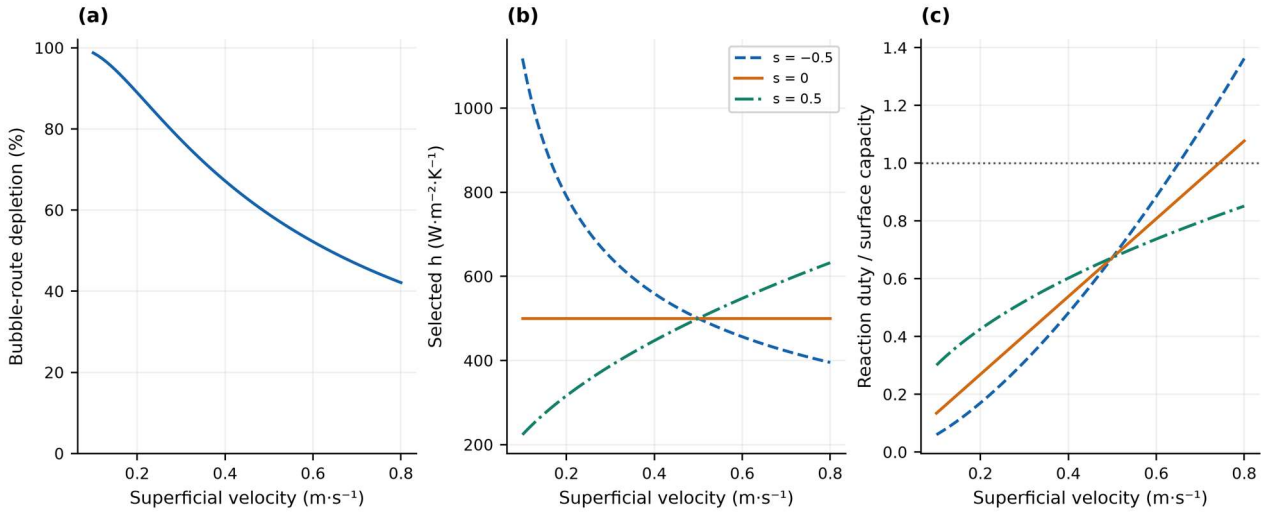


Figure 7. Velocity sensitivity of (**a**) bubble-route depletion, (**b**) assumed heat-transfer coefficients and (**c**) surface-only reaction-duty ratios. The selected curves follow $h = 500(U_0/0.5)^s$ with s = −0.5, 0 and 0.5; they are not experimental fits. H = 0.4 m, T = 650 °C, immersed surface area = 1.571 m^2 per m^2 plan area and bed-to-wall temperature difference = 300 K. Panel (**c**) assumes 90% capture; its dotted line marks a duty-to-capacity ratio of one. No universal optimum velocity is inferred.

6.4. Dimensionless Diagnostics and Their Definitions

The following quantities are diagnostic combinations of established time-scale, equilibrium and heat-balance concepts. They are not presented as newly discovered similarity laws. Definitions specify the averaging and unit basis so that the groups can be used consistently. Table 11 specifies the dimensionless diagnostics and their unit bases.

Table 11. Dimensionless diagnostics with explicit unit bases. These are established concepts or defined ratios, not new validated scaling laws.

Group	Definition	Meaning and Limits
N_x	$\int(K_{be}/u_b)\,dz$	Dimensionless interphase transfer count; depends on phase closure
Da_g	$k_r\,H/U_0$	k_r·in·s^{-1} is normalized per total bed volume; activity and hold-up are absorbed
Θ	$p_{CO2}/p_{eq}(T)$	Local driving-force ratio; $\Theta > 1$ for forward driving force, no universal outlet target
χ_{rad}	h_{rad}/h_{total}	Defined radiation fraction; requires a consistent decomposition
Φ	$Q_{surface,required}/(h\,A_{ht}\,\Delta T)$	Dimensionless surface feasibility ratio; for reaction-only volumetric duty q‴/(h·a·ΔT)

A fast emulsion sink requires an effective reaction rate sufficiently large relative to both exchange and emulsion residence time; comparing Damköhler and transfer numbers alone is not enough when their reference times differ. A positive driving force requires $p_{CO2} > p_{eq}$ locally, whereas the required margin depends on the capture target and kinetics. The thermal duty ratio must be evaluated on matching area or volume bases. None of these checks replaces validation of a coupled model.

7. Research Gaps and Roadmap

7.1. Priority Experimental Gaps

(A) Simultaneous hot-bed measurements. A proposed campaign would use a reacting CaO bed with an instrumented immersed tube and synchronised acquisition of differential pressure, local phase-probe signals, inlet/outlet gas composition, gas flow and temperature. High-temperature capacitance or suitably protected optical probes can provide local bubble-interception statistics, subject to calibration and fouling checks. Molignano et al. [8,9] provide methods and evidence from hot dense beds; the latter combines hydrodynamic measurements with catalytic CO oxidation and is not a CaL experiment.

(B) Identifiable exchange measurements. Inlet and outlet CO_2 should be accompanied by an inert tracer or independently measured outlet molar flow to account for gas contraction. Small nonreactive tracer pulses, introduced under the same hydrodynamic conditions, can constrain gas residence times. Combining two-point phase probes with tracer-response fitting can estimate bubble transit and effective exchange, but chord-to-volume-diameter conversion, bubble phase assignment, and K_{be} remain model-dependent inversions. Their calibration and parameter covariance must be reported.

(C) Particle-state measurements. Repeated quenched samples should determine carbonate fraction by an independently calibrated method, with size distribution, envelope/apparent density, skeletal density and porosity reported separately. Sampling is time-discrete and may not represent the instantaneous local conversion distribution. Emissivity tests should use the same conversion states and thermal histories as the reactor campaign.

(D) Thermal measurements. Calorimetry from coolant mass flow and inlet/outlet enthalpy gives integrated heat duty. Local surface and bed temperatures, together with embedded thermocouples or calibrated heat-flux sensors, can estimate circumferential heat flux. Local h inferred from an inverse conduction model must be distinguished from directly measured duty; radiation and wall conduction require explicit correction. Runs with tubes removed and with alternative pitches would isolate the consequences of internals.

(E) Validation sequence. First establish mass and energy closure and probe response in a nonreacting hot bed; then repeat carbonation at controlled initial conversion and cycle number, with at least two depths and two gas velocities. Use separate datasets for closure fitting and prediction, and compare not only total capture but bubble/chord distributions, pressure spectra, axial CO_2, sampled conversion and heat duty. Finally, test a multistage arrangement with measured interstage composition and solids exchange. This is a proposed protocol, not a report of new experiments.

7.2. The Scaling Problem

Glicksman-type similarity provides a useful starting point for a cold hydrodynamic model, especially geometric ratios, U_0/U_{mf}, a Froude number such as $U_0^2/(gH)$, solids-to-gas density ratio, and particle shape and size distribution [80]. Horio et al. [81] additionally relate similarity to bubble coalescence, splitting and interstitial flow; they also discuss conditions for chemical similarity. Neither should be described as intrinsically incapable of treating reaction. The issue is whether the chosen similarity assumptions remain satisfied along a changing CaL bed.

Preserve the column, distributor, and tube-bank geometry ratios, and bracket the measured particle density and size distribution for calcined, partly carbonated, and cycled states.

Match the hydrodynamic groups at a stated reference state and check their variation along the reactor. A cold bed cannot automatically reproduce reactive gas contraction; imposed changes in gas throughput can test hydrodynamic sensitivity but do not provide full reactive similarity.

Temperature-dependent cohesion and radiative transfer require separate hot tests. Matching density ratio or U_0/U_{mf} alone cannot reproduce these effects.

Particle-state distributions should be propagated into ranges of similarity groups. Thermal driving force, reaction-to-transport timescale ratios, and the equilibrium ratio must then be tested in reacting pilot operation.

The practical scale-up path is consequently staged: cold models screen geometry and flow distribution, hot nonreacting tests constrain thermal and cohesion effects, and reacting pilots test species, energy and sorbent-population coupling. Any unmatched dimensionless groups should be listed with a sensitivity bound. This programme seeks validated reactive similarity for the chosen CaL configuration rather than assuming a universal scaling law.

7.3. Modelling Roadmap

Use independently validated reaction and heat-transfer submodels in 3D TFM or CFD-DEM, and test integrated predictions against separate reacting datasets.

Account for gas consumption or generation in axial flow and bubble closures, while retaining conservation of total and species molar flows.

Represent conversion-dependent particle mass and envelope volume separately; increase population-balance resolution only when measured PSD and conversion distributions justify it.

Evaluate multistage concepts with explicit gas redistribution, per-stage inventories, solids routing, pressure loss and heat removal; equal total bed depth alone is not an equal-design comparison.

Publish assumptions, equations, executable calculation scripts and plotting data for all numerical illustrations, distinguishing sensitivity scenarios from calibrated predictions.

7.4. Design Implications and Limits

The reviewed evidence supports the following conditional design checks.

Compare a single bed, redistributed stages, and a bed with immersed internals using consistent total inventory, gas feed, sorbent supply, and heat duty. Stage depths of 0.2–0.5 m are candidate geometries for testing, not validated general recommendations.

Specify tube-bank geometry in both the thermal and hydrodynamic models, and measure its effect on solids flow, local heat transfer and gas contacting.

Assess the temperature profile against equilibrium and finite kinetics. Axial temperature grading is a possible design variable; the cited MW-scale demonstrations are not used here as proof that a particular grading strategy is necessary or has been optimized for a BFB.

Scale with independently checked transport and solids-circulation assumptions as well as kinetic data. Retain sensitivity to internals, particle-property evolution, and gas-flow contraction.

Assess distributor jets and return-leg conditions against measured sorbent attrition and acceptable pressure drop. No universal exponential attrition dependence is assumed.

Select sorbents using capacity, cyclic reactivity, particle strength, size distribution and hot fluidization behaviour together; chemical improvement does not imply either improved or degraded hydrodynamics without supporting measurements.

8. Conclusions

Bubbling beds are relevant to several CaL applications, but their suitability is duty specific. Earlier coupled multiphase and CaL reactor models already connect transport, reaction, and thermal design. This review contributes a critical comparison and a reproducible set of conditional screening calculations, rather than a claim of first coupling these processes.

Conversion and cycling can change particle properties and fluidization. A constant-envelope calculation illustrates one possible density path, whereas measured bulk density, fragmentation, and conversion-

dependent U_{mf} describe different observables. A population of particles with evolving size, conversion, and cycle history is a more appropriate interpretation than a deterministic Geldart trajectory for every particle.

Capture efficiencies must be defined on a molar-flow basis. The corrected equilibrium calculation includes gas contraction and compares thermodynamic representations at low partial pressure. Temperature and finite reaction rate must be evaluated together, especially for dilute feed streams.

Predicted exchange-limited capture depends strongly on bubble size, but also on correlation choice, size distribution, phase flow partition, and the interchange closure. The sensitivity calculations do not establish bubble diameter as universally more important than sorbent activity or supply.

Staging and immersed internals can improve modelled contacting when they restrict bubble growth. Their benefits depend on redistribution, solids inventory, pressure drop, and thermal integration; no universal stage depth or industrial capture ceiling follows from the present calculation.

The worked heat balance links reaction duty to a specified tube arrangement and to gas and solids sensible heat. It demonstrates conditional geometric and thermal feasibility. The same internals alter the bubble field and solids motion, so a satisfactory area calculation alone does not validate reactor performance.

Heat transfer is regime dependent. Radiation fractions reported for different materials and temperatures should not be combined into a single uncertainty range for a CaL carbonator. A larger gas velocity or more vigorous bubbling does not necessarily increase the total heat-transfer coefficient.

The four-constraint representation is useful for screening only when the operating basis and closures are consistent. The illustrative coupled calculation shows why finite kinetics and thermal feedback can reduce capture below separately calculated limiting values.

The most restrictive constraint can change with inventory, gas composition, particle history, exchanger design, and scale. Such changes should be diagnosed from measurements and coupled balances instead of assigned to scale or sorbent deactivation by default.

A useful next experimental step is to simultaneously measure bubble statistics, inlet and outlet gas flows and composition, solids conversion, and local surface heat flux in a hot reacting bed. Direct observables should be distinguished from inferred interchange coefficients and model-dependent bubble diameters. These data can test the screening assumptions and support subsequent scale-up.

Supplementary Materials

The following supporting information can be found at: https://www.sciepublish.com/article/pii/1303. The Supplementary Information includes Figure S1, Illustrative tube-bank geometry and signed heat-balance scenarios; Table S1, Established CaL model precedents and scope of transfer to the present review; Table S2, Targeted query families used on 27 September 2026; Table S3, Classification of relations and contributions; Table S4, Calculated property propagation at the fixed-envelope baseline; Table S5, Common-initial-diameter comparison at H = 1 m; Table S6, Staging screen at a common total depth of 1 m; Table S7, Coupled-model comparison for the selected effective-rate scenarios; and Table S8, Figure data map. The accompanying data-and-code archive supplies the figure and table data, calculation and plotting scripts, numerical checks and source-access records.

Statement of the Use of Generative AI and AI-Assisted Technologies in the Writing Process

During the preparation of this manuscript, the author used OpenAI for drafting, calculation checks. After using this tool/service, the author(s) reviewed and edited the content as needed and take(s) full responsibility for the content of the published article.

Author Contributions

Conceptualization, Methodology, Software, Formal Analysis, Investigation, Data Curation, Writing Original Draft Preparation, Writing Review and Editing, and Visualization, A.A.

Ethics Statement

Not applicable.

Informed Consent Statement

Not applicable.

Data Availability Statement

The numerical data, calculation scripts, plotting scripts and verification outputs supporting the illustrative analyses are supplied with the Supplementary Information and accompanying data-and-code archive. No new experimental data were generated.

Funding

This research received no external funding.

Declaration of Competing Interest

The author declares that there are no known competing financial interests or personal relationships that could have appeared to influence the work reported in this paper.

Nomenclature

Symbol	Definition	Unit
A_0	Distributor area per orifice	m^2
Ar	$\rho_g(\rho_{env} - \rho_g)g\, d_p^3/\mu^2$	–
$C_{p,g}$, $C_{p,s}$	Gas molar heat capacity; solids specific heat capacity	$J{\cdot}mol^{-1}{\cdot}K^{-1}$; $J{\cdot}kg^{-1}{\cdot}K^{-1}$
d_b	Volume-equivalent bubble diameter	m
d_p	Representative particle diameter; averaging convention stated in text	m
D	Gas-phase molecular diffusivity	$m^2{\cdot}s^{-1}$
D_t	Bed (column) diameter	m
E	Inlet-to-outlet CO_2 capture on a molar-flow basis	–
f_a	Fraction of particles in the "active" (fast-reaction) regime	–
F_R	Molar circulation rate of Ca	$mol{\cdot}s^{-1}$
$F_{CO2,in}$	Molar flow of CO_2 entering the carbonator	$mol{\cdot}s^{-1}$
g	Gravitational acceleration	$m{\cdot}s^{-2}$
h	Bed-to-surface heat transfer coefficient	$W{\cdot}m^{-2}{\cdot}K^{-1}$
H	Expanded bed height	m
K_{bc}, K_{ce}	Bubble–cloud and cloud–emulsion interchange coefficients	s^{-1}
K_{be}	Overall bubble–emulsion interchange coefficient	s^{-1}
N	Cycle number	–
N_x	Interphase transfer count, integral of K_{be}/u_b over bed height	–
p_{eq}	Equilibrium CO_2 partial pressure over $CaO/CaCO_3$	atm
T_b	Bed temperature	K
u_b	Bubble rise velocity	$m{\cdot}s^{-1}$
U_0	Superficial gas velocity	$m{\cdot}s^{-1}$
U_{mf}	Minimum fluidization velocity	$m{\cdot}s^{-1}$
X_N	CaO conversion at cycle N	–
X_r	Residual conversion	–

y_{CO2}	CO_2 mole fraction	–
δ	Bubble volume fraction of the bed	–
ε_{mf}	Bed voidage at minimum fluidization	–
ε_p	Intraparticle porosity	–
ΔH_r	Enthalpy of carbonation	$J \cdot mol^{-1}$
μ	Gas dynamic viscosity	Pa·s
ρ_g, ρ_{env}	Gas and apparent particle density	$kg \cdot m^{-3}$
τ_{act}	Active space time	s
ψ	Ratio of visible bubble flow to ($U_0 - U_{mf}$)	–
J, G_s, A	Molar flux; solids mass flux; reactor plan area	$mol \cdot m^{-2} \cdot s^{-1}$; $kg \cdot m^{-2}\ s^{-1}$; m^2
E_b	Bubble-stream depletion metric for the ideal fast sink	–
$E_{h,0}$	Ideal total-flow transport screen at zero equilibrium concentration	–
a, A_{ht}	Heat-transfer area per bed volume; total immersed surface area	$m^2 \cdot m^{-3}$; m^2
k_r	Effective first-order rate coefficient per total bed volume	s^{-1}
F_0, n_{Ca}	Calcium make-up rate; calcium inventory	$mol \cdot s^{-1}$; mol
ρ_{env}, ρ_{sk}, ρ_{bulk}	Envelope, skeletal and bed bulk density	$kg \cdot m^{-3}$
α	Diameter relative to the reference particle	–
Y, I	CO_2/inert molar ratio; conserved inert molar flux	–; $mol \cdot m^{-2} \cdot s^{-1}$
χ_{rad}, Φ	Radiative fraction; required-to-available surface duty ratio	–
Da_g, Θ	Gas-based Damköhler number; local p_{CO2}/p_{eq}	–

References

1. Arias B, Diego M, Abanades J, Lorenzo M, Diaz L, Martínez D, et al. Demonstration of steady state CO_2 capture in a 1.7 MWth calcium looping pilot. *Int. J. Greenhouse Gas Control* **2013**, *18*, 237–245. DOI:10.1016/j.ijggc.2013.07.014
2. Ströhle J, Junk M, Kremer J, Galloy A, Epple B. Carbonate looping experiments in a 1 MWth pilot plant and model validation. *Fuel* **2014**, *127*, 13–22. DOI:10.1016/j.fuel.2013.12.043
3. Briongos JV, Gomez-Hernandez J, Diaz-Heras M, Almendros-Ibanez JA. Generalized volumetric energy balance for directly irradiated bubbling fluidized beds. *Int. J. Heat Mass Transfer* **2025**, *236*, 126313. DOI:10.1016/j.ijheatmasstransfer.2024.126313
4. Criado YA, García R, Abanades JC. Demonstration of CO_2 capture with CaO and $Ca(OH)_2$ in a countercurrent moving bed carbonator pilot. *Chem. Eng. J.* **2024**, *494*, 152945. DOI:10.1016/j.cej.2024.152945
5. Liu Y, Wang F, Chen S, Xiang W. Experimental investigation of operation characteristics of a lab-scale dual fluidized bed by calcium looping process. *Chem. Eng. Sci.* **2024**, *287*, 119771. DOI:10.1016/j.ces.2024.119771
6. Wang H, Li Z, Li Y, Cai N. Reduced-order model for CaO carbonation kinetics measured using micro-fluidized bed thermogravimetric analysis. *Chem. Eng. Sci.* **2021**, *229*, 116039. DOI:10.1016/j.ces.2020.116039
7. Geldart D. Types of gas fluidization. *Powder Technol.* **1973**, *7*, 285–292. DOI:10.1016/0032-5910(73)80037-3
8. Molignano L, Troiano M, Solimene R, Tebianian S, Scala F, Salatino P, et al. Hydrodynamics and mass transfer around active particles in dense gas-fluidized beds. *Fuel* **2023**, *341*, 127590. DOI:10.1016/j.fuel.2023.127590
9. Molignano L, Troiano M, Solimene R, Scala F, Salatino P. Experimental investigation of hydrodynamics and mass transfer in dense fluidized beds. *Chem. Eng. Trans.* **2025**, *117*, 775–780. DOI:10.3303/CET25117130
10. Theologos KN, Markatos NC. Modelling of flow and heat transfer in fluidized catalytic cracking riser-type reactors. *Chem. Eng. Res. Des.* **1992**, *70*, 239–245. Available online: https://dspace.lib.ntua.gr/xmlui/handle/123456789/10741 (accessed on 29 October 2026).
11. Theologos KN, Markatos NC. Advanced modeling of fluid catalytic cracking riser-type reactors. *AIChE J.* **1993**, *39*, 1007–1017. DOI:10.1002/aic.690390610
12. Theologos KN, Nikou ID, Lygeros AI, Markatos NC. Simulation and design of fluid catalytic-cracking riser-type reactors. *AIChE J.* **1997**, *43*, 486–494. DOI:10.1002/aic.690430221
13. Afandi N, Satgunam M, Mahalingam S, Manap A, Nagi F, Liu W, et al. Review on the modifications of natural and industrial waste CaO based sorbent of calcium looping with enhanced CO_2 capture capacity. *Heliyon* **2024**, *10*, e27119. DOI:10.1016/j.heliyon.2024.e27119
14. Odoi-Yorke F. Advancement in calcium looping for carbon capture: A content and bibliometric review of 20 years of research. *Int. J. Energy Res.* **2025**, *2025*, 8796244. DOI:10.1155/er/8796244
15. Shimizu T, Hirama T, Hosoda H, Kitano K, Inagaki M, Tejima K. A Twin Fluid-Bed Reactor for Removal of CO_2 from Combustion Processes. *Chem. Eng. Res. Des.* **1999**, *77*, 62–68. DOI:10.1205/026387699525882

16. Romano MC. Modeling the carbonator of a Ca-looping process for CO_2 capture from power plant flue gas. *Chem. Eng. Sci.* **2012**, *69*, 257–269. DOI:10.1016/j.ces.2011.10.041
17. Charitos A, Rodríguez N, Hawthorne C, Alonso M, Zieba M, Arias B, et al. Experimental Validation of the Calcium Looping CO_2 Capture Process with Two Circulating Fluidized Bed Carbonator Reactors. *Ind. Eng. Chem. Res.* **2011**, *50*, 9685–9695. DOI:10.1021/ie200579f
18. Guo X, Zhou W, Wei J. Numerical simulation of fluidized bed reactor for calcium looping energy release process in thermochemical storage: Influence of key conditions. *Renew. Energy* **2024**, *237*, 121532. DOI:10.1016/j.renene.2024.121532
19. Xue Q, Fox RO. Multi-fluid CFD modeling of biomass gasification in polydisperse fluidized-bed gasifiers. *Powder Technol.* **2014**, *254*, 187–198. DOI:10.1016/j.powtec.2014.01.025
20. Baker EH. The calcium oxide–carbon dioxide system in the pressure range 1–300 atmospheres. *J. Chem. Soc.* **1962**, 464–470. DOI:10.1039/JR9620000464
21. Silcox GD, Kramlich JC, Pershing DW. A mathematical model for the flash calcination of dispersed calcium carbonate and calcium hydroxide particles. *Ind. Eng. Chem. Res.* **1989**, *28*, 155–160. DOI:10.1021/ie00086a005
22. Hornberger M, Moreno J, Schmid M, Scheffknecht G. Experimental investigation of the carbonation reactor in a tail-end Calcium Looping configuration for CO_2 capture from cement plants. *Fuel Process. Technol.* **2020**, *210*, 106557. DOI:10.1016/j.fuproc.2020.106557
23. Bhatia SK, Perlmutter DD. A random pore model for fluid–solid reactions: I. Isothermal, kinetic control. *AIChE J.* **1980**, *26*, 379–386. DOI:10.1002/aic.690260308
24. Bhatia SK, Perlmutter DD. Effect of the product layer on the kinetics of the CO_2–lime reaction. *AIChE J.* **1983**, *29*, 79–86. DOI:10.1002/aic.690290111
25. Ooi BKH, Marek EJ. Kinetics of CO_2 capture with calcium oxide during direct air capture in a fluidized bed. *Energy Fuels* **2024**, *38*, 22290–22297. DOI:10.1021/acs.energyfuels.4c03770
26. Martinez J, Wardini JL, Zheng X, Moghimi L, Rakowsky J, Means J, et al. Precision calcination mechanism of $CaCO_3$ to high-porosity nanoscale CaO CO_2 sorbent revealed by direct *in situ* observations. *Adv. Mater. Interfaces* **2024**, *11*, 2300811. DOI:10.1002/admi.202300811
27. Cai J, Li Z. First principle-based rate equation theory for the calcination kinetics of $CaCO_3$ in calcium looping. *Energy Fuels* **2024**, *38*, 8145–8156. DOI:10.1021/acs.energyfuels.4c00877
28. Asiedu-Boateng P, Asiedu NY, Patience GS, McDonough JR, Zivkovic V. High temperature micro fluidization of limestones. *Particuology* **2026**, *108*, 156–167. DOI:10.1016/j.partic.2025.10.020
29. Grasa GS, Abanades JC. CO_2 capture capacity of CaO in long series of carbonation/calcination cycles. *Ind. Eng. Chem. Res.* **2006**, *45*, 8846–8851. DOI:10.1021/ie0606946
30. Tizfahm M, Tahmasebpoor M, Ramezan Behtash H, Balsamo M, Montagnaro F. Coupled kinetic and hydrodynamic model for a carbonator reactor of calcium looping process: Sulfur dioxide effect. *Process Saf. Environ. Prot.* **2024**, *185*, 1205–1218. DOI:10.1016/j.psep.2024.03.065
31. Anthony EJ, Granatstein DL. Sulfation phenomena in fluidized bed combustion systems. *Prog. Energy Combust. Sci.* **2001**, *27*, 215–236. DOI:10.1016/S0360-1285(00)00021-6
32. Coppola A, Montagnaro F, Salatino P, Scala F. Fluidized bed calcium looping: The effect of SO_2 on sorbent attrition and CO_2 capture capacity. *Chem. Eng. J.* **2012**, *207–208*, 445–449. DOI:10.1016/j.cej.2012.06.149
33. Bai R, Li N, Liu Q, Chen S, Liu Q, Zhou X. Effect of steam on carbonation of CaO in Ca-looping. *Molecules* **2023**, *28*, 4910. DOI:10.3390/molecules28134910
34. Krödel M, Leroy C, Kim SM, Naeem MA, Kierzkowska A, Wu YH, et al. Of glasses and crystals: Mitigating the deactivation of CaO-based CO_2 sorbents through calcium aluminosilicates. *JACS Au* **2023**, *3*, 3111–3126. DOI:10.1021/jacsau.3c00475
35. Vijayaraghavan Ramesh A, Hashemi SM, Mahinpey N. CO_2 capture with Mg-, Al-, and Zr-assisted CaO-based sorbents in the calcium looping process under mild and realistic conditions. *Ind. Eng. Chem. Res.* **2025**, *64*, 6114–6127. DOI:10.1021/acs.iecr.4c04749
36. Groh D, Chmielniak P, Jones CW, Sievers C. Process enhancement of calcium looping through combined mechanical and chemical sorbent reactivation. *ChemSusChem* **2025**, *18*, e202500835. DOI:10.1002/cssc.202500835
37. Wen CY, Yu YH. A generalized method for predicting the minimum fluidization velocity. *AIChE J.* **1966**, *12*, 610–612. DOI:10.1002/aic.690120343
38. Tregambi C, Di Lauro F, Pascual S, Lisbona P, Romeo LM, Solimene R, et al. Solar-driven calcium looping in fluidized beds for thermochemical energy storage. *Chem. Eng. J.* **2023**, *466*, 142708. DOI:10.1016/j.cej.2023.142708

39. Di Lauro F, Tregambi C, Montagnaro F, Molignano L, Salatino P, Solimene R. Influence of fluidised bed inventory on the performance of limestone sorbent in calcium looping for thermochemical energy storage. *Energies* **2023**, *16*, 6942. DOI:10.3390/en16196942
40. Darton RC, LaNauze RD, Davidson JF, Harrison D. Bubble growth due to coalescence in fluidised beds. *Trans. Inst. Chem. Eng.* **1977**, *55*, 274–280.
41. Mori S, Wen CY. Estimation of bubble diameter in gaseous fluidized beds. *AIChE J.* **1975**, *21*, 109–115. DOI:10.1002/aic.690210114
42. Werther J. Effect of gas distributor on hydrodynamics of gas fluidized beds. *Ger. Chem. Eng.* **1978**, *1*, 166–174.
43. Jaiswal R, Moldestad BME, Eikeland MS, Nielsen HK, Thapa RK. Image Processing and Measurement of the Bubble Properties in a Bubbling Fluidized Bed Reactor. *Energies* **2022**, *15*, 7828. DOI:10.3390/en15217828
44. Yang Z, Mazza G, Vanierschot M, Ansart R, Deng Y. Experimental and CFD investigation of bubble dynamics in Geldart group B fluidized beds: A comparative 2D and 3D analysis. *Appl. Sci.* **2026**, *16*, 6372. DOI:10.3390/app16136372
45. Davidson JF, Harrison D. *Fluidised Particles*; Cambridge University Press: Cambridge, UK, 1963.
46. Cai M, Niu L, Yang H, Xu W, Liu M, Lu C. Experimental investigation on bubble and agglomerate behaviors of Geldart B particles in a 3D gas–solid fluidized bed reactor. *Ind. Eng. Chem. Res.* **2024**, *63*, 3301–3312. DOI:10.1021/acs.iecr.3c04080
47. Bai T, Sun Z, Guo Z, Zhu J, Barghi S. Bubble dynamics in a binary gas–solid fluidization system of Geldart B and Geldart D particles. *Chem. Eng. Sci.* **2022**, *258*, 117771. DOI:10.1016/j.ces.2022.117771
48. Wu K, Francia V, Jiang S, Coppens MO. An experimental flow regime map to dynamically structure gas-solid bubbling fluidized beds. *AIChE J.* **2025**, *71*, e18681. DOI:10.1002/aic.18681
49. Xie J, Gao H, Zhang Q, Chen J, Wang Z, Zhang C, et al. Characteristics of mass transfer between bubble and emulsion phases of high-temperature gas-solid bubbling fluidized beds. *Particuology* **2025**, *107*, 26–34. DOI:10.1016/j.partic.2025.09.014
50. Jiang S, Wu K, Francia V, Ouyang Y, Coppens MO. Machine learning assisted experimental characterization of bubble dynamics in gas-solid fluidized beds. *Ind. Eng. Chem. Res.* **2024**, *63*, 8819–8832. DOI:10.1021/acs.iecr.4c00631
51. Ding J, Gidaspow D. A bubbling fluidization model using kinetic theory of granular flow. *AIChE J.* **1990**, *36*, 523–538. DOI:10.1002/aic.690360404
52. Theologos KN, Maroulis ZB, Markatos NC. Simulation of transport dynamics in fluidized-bed dryers. *Drying Technol.* **1997**, *15*, 1269–1291. DOI:10.1080/07373939708917295
53. Tsuji Y, Kawaguchi T, Tanaka T. Discrete particle simulation of two-dimensional fluidized bed. *Powder Technol.* **1993**, *77*, 79–87. DOI:10.1016/0032-5910(93)85010-7
54. Kaneko Y, Shiojima T, Horio M. DEM simulation of fluidized beds for gas-phase olefin polymerization. *Chem. Eng. Sci.* **1999**, *54*, 5809–5821. DOI:10.1016/S0009-2509(99)00153-0
55. Wang S, Shen Y. Coarse-grained CFD-DEM modelling of dense gas-solid reacting flow. *Int. J. Heat Mass Transfer* **2022**, *184*, 122302. DOI:10.1016/j.ijheatmasstransfer.2021.122302
56. Song C, Che J, Yang X, Wang R, Li Y. Multi-scale simulation for energy release performance of carbonation process in solar-driven calcium-looping: From grain to reactor. *Renew. Sustain. Energy Rev.* **2025**, *210*, 115202. DOI:10.1016/j.rser.2024.115202
57. Song C, Guo Q, Li Y, Che J, Fang J, Xu Q, et al. Dynamically structured bubbles enhance energy release performance in solar-driven carbonation reaction. *Chem. Eng. J.* **2026**, *543*, 177976. DOI:10.1016/j.cej.2026.177976
58. Mickley HS, Fairbanks DF. Mechanism of heat transfer to fluidized beds. *AIChE J.* **1955**, *1*, 374–384. DOI:10.1002/aic.690010317
59. Baskakov AP, Berg BV, Vitt OK, Filippovsky NF, Kirakosyan VA, Goldobin JM, et al. Heat transfer to objects immersed in fluidized beds. *Powder Technol.* **1973**, *8*, 273–282. DOI:10.1016/0032-5910(73)80092-0
60. Botterill JSM. *Fluid-Bed Heat Transfer*; Academic Press: London, UK, 1975.
61. Grewal NS, Saxena SC. Heat transfer between a horizontal tube and a gas–solid fluidized bed. *Int. J. Heat Mass Transfer* **1980**, *23*, 1505–1519. DOI:10.1016/0017-9310(80)90154-4
62. Martin H. Heat transfer between gas fluidized beds of solid particles and the surfaces of immersed heat exchanger elements, part I. *Chem. Eng. Process.* **1984**, *18*, 157–169. DOI:10.1016/0255-2701(84)80005-7
63. Molerus O, Wirth KE. *Heat Transfer in Fluidized Beds*; Chapman & Hall: London, UK, 1997. DOI:10.1007/978-94-011-5842-8
64. Glicksman LR. Scaling relationships for fluidized beds. *Chem. Eng. Sci.* **1984**, *39*, 1373–1379. DOI:10.1016/0009-2509(84)80070-6

65. Yoshida K, Ueno T, Kunii D. Mechanism of bed–wall heat transfer in a fluidized bed at high temperatures. *Chem. Eng. Sci.* **1974**, *29*, 77–82. DOI:10.1016/0009-2509(74)85032-3
66. Stenberg V, Sköldberg V, Öhrby L, Rydén M. Evaluation of bed-to-tube surface heat transfer coefficient for a horizontal tube in bubbling fluidized bed at high temperature. *Powder Technol.* **2019**, *352*, 488–500. DOI:10.1016/j.powtec.2019.04.073
67. Chen Z, Gao H, Zhang Q, Li T, Fu L, Xu G, et al. Understanding heat transfer and the role of bed hydrodynamics in high-temperature fluidized beds. *Ind. Eng. Chem. Res.* **2025**, *64*, 854–867. DOI:10.1021/acs.iecr.4c03348
68. Guo X, Cu W, Zheng N, Zhou W, Wei J. Numerical simulation of hydrodynamics and heat transfer in a bubbling fluidized bed with horizontally immersed tubes and Geldart B particles. *Int. J. Heat Mass Transfer* **2026**, *254*, 127718. DOI:10.1016/j.ijheatmasstransfer.2025.127718
69. Sattari F, Tahmasebpoor M, Valverde JM, Ortiz C, Mohammadpourfard M. Modelling of a fluidized bed carbonator reactor for post-combustion CO_2 capture considering bed hydrodynamics and sorbent characteristics. *Chem. Eng. J.* **2021**, *406*, 126762. DOI:10.1016/j.cej.2020.126762
70. Abanades JC. The maximum capture efficiency of CO_2 using a carbonation/calcination cycle of CaO/$CaCO_3$. *Chem. Eng. J.* **2002**, *90*, 303–306. DOI:10.1016/S1385-8947(02)00126-2
71. Abanades JC, Alvarez D. Conversion limits in the reaction of CO_2 with lime. *Energy Fuels* **2003**, *17*, 308–315. DOI:10.1021/ef020152a
72. Lasheras A, Ströhle J, Galloy A, Epple B. Carbonate looping process simulation using a 1D fluidized bed model for the carbonator. *Int. J. Greenhouse Gas Control* **2011**, *5*, 686–693. DOI:10.1016/j.ijggc.2011.01.005
73. Diego ME, Arias B, Abanades JC. Modeling the solids circulation rates and solids inventories of an interconnected circulating fluidized bed reactor system for CO_2 capture by calcium looping. *Chem. Eng. J.* **2012**, *198–199*, 228–235. DOI:10.1016/j.cej.2012.05.099
74. Ylätalo J, Ritvanen J, Arias B, Tynjälä T, Hyppänen T. 1-Dimensional modelling and simulation of the calcium looping process. *Int. J. Greenh. Gas Control* **2012**, *9*, 130–135. DOI:10.1016/j.ijggc.2012.03.008
75. Hawthorne C, Charitos A, Perez-Pulido CA, Bing Z, Scheffknecht G. Design of a dual fluidised bed system for the post-combustion removal of CO_2 using CaO. Part I: CFB carbonator reactor model. In Proceedings of the 9th International Conference on Circulating Fluidized Beds, Hamburg, Germany, 13–16 May 2008; pp. 759–764.
76. Moghtaderi B, Seyfaee A. A multi-scale experimental study on calcium-looping for thermochemical energy storage using the CO_2 captured from power generation systems. *J. Energy Storage* **2024**, *86*, 111400. DOI:10.1016/j.est.2024.111400
77. Kunii D, Levenspiel O. Bubbling Bed Model. Model for Flow of Gas through a Fluidized Bed. *Ind. Eng. Chem. Fundam.* **1968**, *7*, 446–452. DOI:10.1021/i160027a016
78. Kunii D, Levenspiel O. *Fluidization Engineering*, 2nd ed.; Butterworth-Heinemann: Boston, MA, USA, 1991. DOI:10.1016/C2009-0-24190-0
79. Marques LM, Mota SM, Teixeira P, Mateus M, Pinheiro CIC. Decarbonisation of cement industry: Calcium looping with white mud and limestone as CaO-based sorbents for industrial flue gas treatment. *Chem. Eng. Process.* **2025**, *213*, 110290. DOI:10.1016/j.cep.2025.110290
80. Glicksman LR, Hyre M, Woloshun K. Simplified scaling relationships for fluidized beds. *Powder Technol.* **1993**, *77*, 177–199. DOI:10.1016/0032-5910(93)80055-F
81. Horio M, Nonaka A, Sawa Y, Muchi I. A new similarity rule for fluidized bed scale-up. *AIChE J.* **1986**, *32*, 1466–1482. DOI:10.1002/aic.690320908